Graduate School of Frontier Sciences, The University of Tokyo
Department of Socio-Cultural Environment Studies

2021
Master's Thesis

Time series estimation of CO2 exchange during winter and spring at Urayasu in Tokyo Bay
東京湾の浦安における冬から春にかけての CO2 交換の時系列推定

Submitted on July 9, 2021
Advisor: Professor Jun SASAKI

Jia, Hanchen
賈 漢辰

Contents

List of Figures

List of Tables

Chapter 1　Introduction

1.1 Research background

In recent decades, widespread impacts on human and natural systems induced by observed global warming, which is reported to be caused by the massive emissions of anthropogenic greenhouse gases largely driven by economic and population growth, indicated the sensitivity of natural and human systems to changing climate. The atmospheric concentrations of greenhouse gas, including carbon dioxide, methane, nitrous oxide has already been at an unprecedented high level in at least the last 800,000 years, and the continuing emission of GHG may further increase the likelihood of pervasive and irreversible impacts for people and ecosystems. Under this background, substantial and sustained reductions in GHG is regarded as the approach to limit climate change risks[1].

Utilizing the ability of forests and oceans to absorb CO2 is a crucial countermeasure for climate change mitigation. The forests no doubt contributes massively to burying carbon, but the role of the oceans in carbon sequestration was once overlooked. In fact, of all the annually captured green carbon, the carbon captured by photosynthetic activity, over half (55%) is captured by marine living organisms. The oceans, though only holds 0.05% of the plant biomass on land, cycles almost the same amount of carbon per year, demonstrating extreme efficiency in carbon sinking. This carbon absorbed and fixed in the ocean from atmospheric CO2 is defined as ocean blue carbon[2].

Ocean blue carbon is primarily fixed through three marine carbon pumps: the physical pump dissolves atmospheric CO2 into seawater, the biological pump absorbs and transforms CO2 through photosynthesis of marine phytoplankton and deposited into the seabed, the marine carbonate pump is absorbed and released by marine organisms like shellfish and coral reefs[1, 3]. By contrast, the coastal blue carbon was defined narrowly as the carbon sequestered in vegetated coastal ecosystems, in particular mangroves, salt marshes, and seagrasses[3]. These vegetated habitats are indeed the most crucial, climate-combating habitats, ranking among the most intense carbon sinks on the planet. Although they occupy only 0.2% of the ocean surface, 50% of carbon burial in marine sediments was contributed, and are responsible for storing up to some 70% of the carbon permanently in the marine realm, in part because of their efficiency in trapping suspended matter and associated organic carbon during tidal inundation[2, 3]. Besides, they also function to buffer the impacts of rising sea levels and wave action associated with climate change with their canopies or high burial rates to raise the seafloor[4]. The mentioned high productivity and functionality was considered as the underlying reason for the narrow definition of coastal blue carbon.

Recently, attempts have been made to extend the previous definition of coastal blue carbon-based on functionality, to a broad sense based on the scientific processes of the carbon cycle in the coastal zone, that broad definition of coastal blue carbon refers to the carbon absorbed from atmospheric CO2 and converted by the higher plants in coastal ecosystems, phytoplankton, algae, and calcifier organisms and then buried in the sediments for the long term under the combined effect of plants and microorganisms[5]. In this sense, grasping the CO2 exchange characteristics between sea and air becomes an important mission.

Sea- air CO2 exchange constantly happens, and net CO2 flux tends to sink from atmosphere to ocean due to the increasing CO2 concentration in the atmosphere year by year. Quantification of air-sea CO2 exchange carried out all over the world reveals that marginal seas at high and temperate latitudes act as sinks of CO2, whereas subtropical and tropical marginal seas act as sources of CO2[6], stressing the importance of coastal oceans to integrate CO2 fluxes at the global scale. Particularly, partially enclosed coastal areas like estuaries that locates between 23.5 and $50°\mathrm{N}$ with a salinity of more than 25 ppt is deemed to have a large potential to absorb CO2 [7], thus as an important location for CO2 reduction, further understanding of the characteristics of CO2 exchange in enclosed coastal areas is desirable.

1.2 Blue carbon in bays

In enclosed coastal water surrounded by highly urbanized areas, the high primary productivity driven by nutrient loading from land effects on the carbon cycle significantly, therefore this coastal water is thought to have the potential in absorbing CO2. In Japan, various studies based on field work has been conducted. As a eutrophicated coastal environment, Osaka Bay is reported to have the potential for CO2 absorption[8], and similarly, extensive surveys indicated that the overall Tokyo bay acts as a strong net sink for atmospheric CO2[9]. However, the blue carbon community's attention is more focused on the coastal ecosystems including mangroves, salt marshes, and seagrasses, thus the function of the bays surrounded by highly urbanized areas needs to be further identified to clarify the importance of eutrophic coastal waters as part of coastal blue carbon.

CO2 flux is determined by the difference between CO2 partial pressure in the atmosphere ($\mathrm{pCO_{2air}}$) and in seawater ($\mathrm{pCO_{2sw}}$). When $\mathrm{pCO_{2air}}$ is higher than the surface $\mathrm{pCO_{2sw}}$, CO2 is absorbed and vice versa, but the $\mathrm{pCO_{2sw}}$ in coastal seas varies due to many factors, such as photosynthesis, respiration, chemical equilibrium, stratification, and upwelling[8, 10, 11]. Hence, time-series monitoring is considered as an effective approach to capture the environmental change, and at the same time reflect the influence of water environment change on $\mathrm{pCO_{2sw}}$.

Additionally, the seawater carbonate system has also been studied. The highly linear relation between total alkalinity ($\mathrm{A_T}$), which measures the water's ability to neutralize acids, and salinity was found in Tokyo Bay, Osaka Bay, and Ise Bay[12], due to the fact that when the ion composition ratio of seawater is constant, the $\mathrm{A_T}$ is proportional to the salinity. Based on this finding, the previous method for $\mathrm{pCO_{2sw}}$ estimation first estimate $\mathrm{A_T}$ from salinity then use this estimated $\mathrm{A_T}$ along with field measured pH to calculate the $\mathrm{pCO_{2sw}}$. Nevertheless, given that the $\mathrm{A_T}$-salinity relationship varies from place to place[13], and that no-linear relationship was found between these two terms[14], the accuracy of this linear $\mathrm{A_T}$-salinity equation for Tokyo Bay developed with merely 59 samples is doubtful. In this study, the developed $\mathrm{A_T}$-salinity linear relation was found may not be robust enough to estimate $\mathrm{A_T}$ in the river mouth. Also, the previous method of using field measured pH and estimated $\mathrm{A_T}$ as input to CO2SYS[15] is found resulting in an underestimation in pCO2sw.

1.3 Research objectives

This research aims to develop a generalized estimation method of $\mathrm{pCO_{2sw}}$ and $\mathrm{A_T}$ appliable in a river mouth at the head of the Tokyo Bay based on a monitoring dataset. $\mathrm{A_T}$ estimation model is developed to complement the shortcoming of the $\mathrm{A_T}$-S regression equation developed in 2009 that may not be able to predict on $\mathrm{A_T}$ at locations influenced by river water. The generalized estimation method of $\mathrm{pCO_{2sw}}$is an improvement to the traditional way of using CO2SYS[15] to estimate the field $\mathrm{pCO_{2sw}}$.

Meanwhile, time-series field observation is conducted in Urayasu to fill in the gap of completely missing night-time seawater carbonate system data in Tokyo Bay; also, the survey's time span from winter to spring reflects the influence of phytoplankton activity and the location reflects the river water inflow influence on seawater carbonate system to further figure out functions of urbanized bays as blue carbon.

1.4 Chemistry of carbon dioxide in seawater

The solution chemistry of carbon dioxide in seawater, which is considered as the basis of this study, is described in this section. Referring to Dickson's textbook[16, 17].

1.4.1 Acid-base equilibria of $\mathbf{CO_2}$ in seawater

When carbon dioxide dissolves in seawater, it can be considered to react with the water in the following series of chemical equilibria:

$$\mathrm{CO_2(g)} \rightleftharpoons \mathrm{CO_2^*(aq)} \tag{1.1}$$

$$\mathrm{CO_2^*(aq) + H_2O(l) \rightleftharpoons H^+(aq) + HCO_3^-(aq)} \tag{1.2}$$

$$\mathrm{HCO_3^-(aq) \rightleftharpoons H^+(aq) + CO_3^{2-}(aq)} \tag{1.3}$$

The notations (g), (l), and (aq) refer to the gas state, liquid state, and aqueous solution state, respectively. Equation (1.1) describes the solubility equilibrium of carbon dioxide between air and seawater; equations (1.2) and (1.3) describe consecutive acid dissociation reactions of dissolved carbon dioxide. $\mathrm{CO_2^*(aq)}$ in equation(1.2) is the concentration of a hypothetical species, meaning the sum of the concentration of $\mathrm{CO_2(aq)}$ and $\mathrm{H_2CO_3(aq)}$.

At equilibrium, the concentration of $\mathrm{H_2CO_3}$, is only about 1/1000 of $[\mathrm{CO_2(aq)}]$ with no special significance to the acid-base equilibria, also there is no need to analytically distinguish these two terms so that it is common to use $\mathrm{CO_2^*(aq)}$ in equation (1.1) and (1.2).

The equilibrium relationships between the concentrations of these various species can then be written in terms of the equilibrium constants:

$$K_0 = \frac{[\mathrm{CO_2^*}]}{f(\mathrm{CO_2})} \tag{1.4}$$

$$K_1 = \frac{[\mathrm{H^+}][\mathrm{HCO_3^-}]}{[\mathrm{CO_2^*}]} \tag{1.5}$$

$$K_2 = \frac{[\mathrm{H^+}][\mathrm{CO_3^{2-}}]}{[\mathrm{HCO_3^-}]} \tag{1.6}$$

Where the brackets "[ ]" represent total stoichiometric concentrations of the particular chemical species enclosed between them, expressed as mol/kg of solution. In equation (1.4), $f(\mathrm{CO_2})$ is the fugacity of carbon dioxide in the gas phase.

The fugacity is an effective partial pressure that replaces the mechanical partial pressure in an accurate computation of the chemical equilibrium constant[18]. In this study, the term $\mathrm{pCO_2}$-- the partial pressure of CO2 in the gas phase is used to replace $f(\mathrm{CO_2})$ as in equation (1.7), for the reason that the difference between $f(\mathrm{CO_2})$ and $\mathrm{pCO_2}$ is very tiny that multiple studies use $f(\mathrm{CO_2})$ equally as $\mathrm{pCO_2}$. Both $f(\mathrm{CO_2})$and $\mathrm{pCO_2}$ are proportional to the dissolved $\mathrm{CO_2}$. The fugacity is about 0.3% to 0.4% lower than the partial pressure over the range of interest, due to the nonideality of CO2[19].

$$K_0 = \frac{[\mathrm{CO_2^*}]}{\mathrm{pCO_2}} \tag{1.7}$$

The above equilibrium constants are functions of the temperature and salinity of sea water and have been measured in various studies.

$$\begin{aligned}\ln(\mathrm{K_0/k^o}) &= 93.4517 \times \left(\frac{100}{\mathrm{T}}\right) - 60.2409 + 23.3585 \times \ln\left(\frac{\mathrm{T}}{100}\right) \\ &\quad + \mathrm{S}(0.023517 - 0.023656 \times \left(\frac{\mathrm{T}}{100}\right) + 0.0047036 \times \left(\frac{\mathrm{T}}{100}\right)^2)\end{aligned} \tag{1.8}$$

$$\begin{aligned}\log\left(\frac{\mathrm{K_1}}{\mathrm{k^o}}\right) &= \frac{-3633.86}{\mathrm{T}} + 61.2172 - 9.67770 \ln(\mathrm{T}) + 0.011555\ \mathrm{S} \\ &\quad - 0.0001152\ \mathrm{S}^2\end{aligned} \tag{1.9}$$

$$\log\left(\frac{K_2}{\mathrm{k^o}}\right) = \frac{-471.78}{T} - 25.9290 + 3.16967 \ln(T) + 0.01781\ S - 0.0001122\ S^2 \tag{1.10}$$

Where T means temperature (°C), and S means salinity (PSU).
$\mathrm{k^o}$= 1 mol / kg;

1.4.2 Analytical parameters for seawater Carbonate System

Measuring the individual concentrations of each acid-base species to get a complete description of the carbon dioxide system of a particular seawater sample is not considered as a practical approach, however, four parameters can be measured instead; they are total alkalinity ($\mathrm{A_T}$), total dissolved inorganic carbon (DIC), hydrogen ion concentration (pH), and the partial pressure of carbon dioxide in the air in equilibrium with a seawater sample ($\mathrm{pCO_2}$).

DIC is the total amount of carbonate, bicarbonate, and dissolved carbon dioxide of a seawater sample, expressed in moles per kilogram of solution (equation 1.11). $\mathrm{A_T}$ is the number of moles of hydrogen ion equivalent to the excess of proton acceptors over proton donors in 1 kilogram of the sample (equation 1.12). pH is also expressed on a total scale in moles per kilogram of solution (equation 1.13). $\mathrm{pCO_2}$ is a measure of the degree of saturation of the sample with $\mathrm{CO_2}$ gas in the unit of μatm.

$$\mathrm{DIC} = [\mathrm{CO_2^*}] + [\mathrm{HCO_3^-}] + [\mathrm{CO_3^{2-}}] \tag{1.11}$$

$$\begin{aligned}\mathrm{A_T} &= [\mathrm{HCO_3^-}] + 2[\mathrm{CO_3^{2-}}] + [\mathrm{B(OH)_4^-}] + [\mathrm{OH^-}] + [\mathrm{HPO_4^{2-}}] + 2[\mathrm{PO_4^{3-}}] + [\mathrm{H_3SiO_4}] \\ &\quad + [\mathrm{NH_3}] + [\mathrm{HS^-}] - [\mathrm{H^+}] - [\mathrm{HSO_4^-}] - [\mathrm{HF}] - [\mathrm{H_3PO_4}]\end{aligned} \tag{1.12}$$

$$\mathrm{pH} = -\log_{10}\{[\mathrm{H^+}] + [\mathrm{HSO_4^-}]\} \tag{1.13}$$

1.5 CO2 flux calculation

CO2 flux F_{CO2} can be calculated from equation 1.14.

$$F_{CO2} = kK_0(pCO_{2\,sw} - pCO_{2\,air}) \tag{1.14}$$

Here the $pCO_{2\,sw}$ refers to the pCO_2 in the surface seawater, and the $pCO_{2\,air}$ means the pCO_2 in the atmosphere. The k term can be calculated form equation 1.15.

$$k = 0.39 \times (660/S_c)^{-0.5} \times {U_{10}}^2 \tag{1.15}$$

Within equation 1.15, U_{10} is the wind speed 10m above the sea surface, while S_c is the Schmidt number, which is computed using equation 1.16.

$$S_c = 2073.1 - 125.62T + 3.6276T^2 - 0.043219T^3 \tag{1.16}$$

Practically, CO2 flux is calculated with the following equation 1.17.

$$\begin{aligned} &F_{CO2}(\mu mol/m^2 \cdot s) \\ &\quad = k \times \frac{0.01}{3600}(m/s) \times K_0(mol/atm \cdot kg) \times \rho_w(kg/m^3) \\ &\quad \times \Delta pCO_2 \ (\mu atm) \end{aligned} \tag{1.17}$$

Here, ρ_w is the density of seawater.
Furthermore, the $pCO_{2\,air}$ is estimated using equation 1.18.

$$pCO_{2\,air}(\mu atm) = (P - e) \times \chi CO_2(ppm) \tag{1.18}$$

χCO_2 means atmospheric carbon dioxide concentration, P means atmospheric pressure (atm), and e is saturated water vapor pressure (atm).

In this study, the $pCO_{2\,air}$ is estimated using the average CO2 concentration measured in 2020 by Japan Meteorological Agency and the average atmospheric pressure measured in our field survey using equation 1.18 ranging from 401 to 415µatm.

Chapter 2 Methodology

2.1 Study site

The continuous sampling station was located at 35°38'02.1"N 139°55'27.2"E, the closest location to the Urayasu monitoring station, also a location in which red tide is supposed to have a high possibility to occur.

Urayasu monitoring station measures and uploads real-time environment parameters including atmospheric temperature, wind velocities, water temperature, salinity, pH, DO, *chlorophyll-a* fluorescence, turbidity, and current velocities at 15 min intervals[20]. This meets the requirement to improve and develop regression equations for $\mathrm{A_T}$ and $\mathrm{pCO_{2sw}}$. The proximity of the sampling spot to the monitoring station also offered extra information about the water environment, therefore facilitating the interpretation of the phenomenon during field surveys.

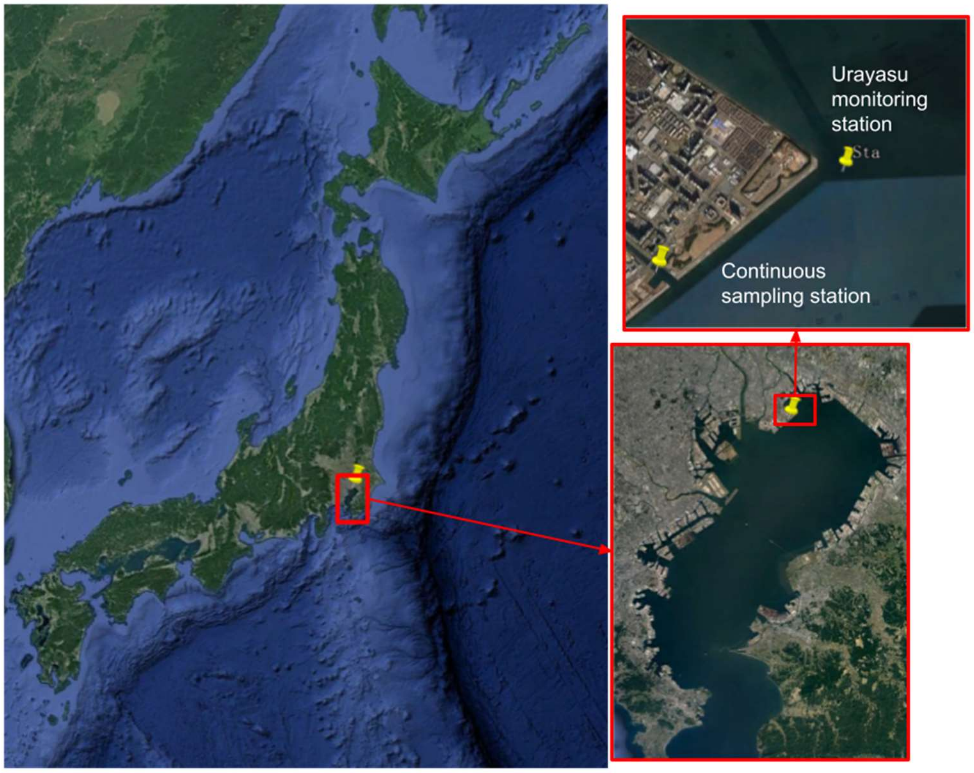

Figure 2.1 Location of the study area; Continuous sampling spot and Urayasu monitoring station. (From Google Earth)

Our continuous sampling location is at the mouth of the Sakai River. A survey was also conducted in the Sakai River to see the river inflow influence.

There are two water gates on Sakai River, the West Water Gate is at the very upstream, controlling the Edo River inflow to Sakai River, the other is the East Water Gate at the middle of Sakai River. We chose the East Water Gate as our survey location, supposing the salinity gradient and therefore the A_T gradient can already be seen here.

Water samples were taken at both upstream (35°39'21.5"N 139°53'56.6"E) and downstream (35°39'13.1"N 139°54'01.8"E) of the watergate.

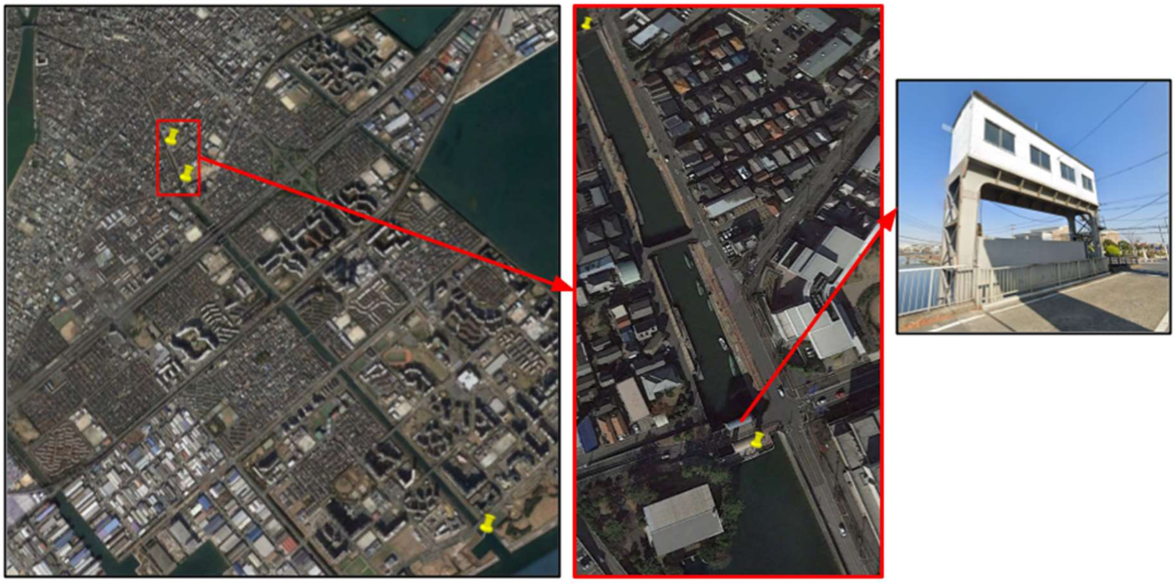

Figure 2.2 Location of the study area; left: River sampling location; right: East water Gate. (From Google Earth)

2.2 Water quality monitoring using mooring system

The sensors listed in Table 2.1 were used to build up the mooring system. Except for the water parameters listed in the table, all the sensors can measure water temperature.

Table 0.1 HOBO Onset sensors used for mooring system

U20L-04	Water Level (0-4 m) Data Logger
U20L-02	Water Level (0-30.6 m) Data Logger
U26 -001	Dissolved Oxygen Data Logger
U24-002-C	Saltwater Conductivity/Salinity Data Logger

MX2501	pH Data Logger

One set of sensors measuring water level, EC, DO and pH were attached to a rod that stands vertically on a weight 0.5m away from the bottom. The other set of sensors measuring the same water parameters was attached to the rope 0.5 m below the water surface by connecting to a buoy. One additional water level sensor is attached to the rope and above the water surface, the rope is tied to a guard rail on the bank. By subtracting atmospheric pressure from the water pressure, sensor depth can be calculated.

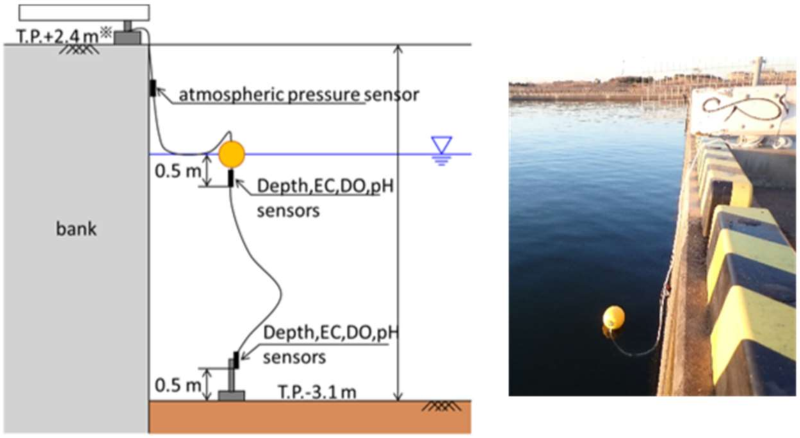

Figure 2.3 Mooring System; left: Schematic diagram, right: System set in the field

2.3 Water quality measurement and water sampling

In order to minimize gas exchange with the atmosphere (CO2 exchange affects various carbon parameters to different degrees, among which, $\mathrm{pCO}_{2\mathrm{sw}}$ is the most sensitive one and alkalinity is less affected [17]), the following sampling process is adopted using equipment in Table 2.2.

Direct reading water quality meter AAQ and water sampler are connected with vinyl tape that the water parameters can be measured at the moment when a water sample is taken, as shown in Figure 2.4. Before transferring seawater sample from sampler to bottles, silicon tube is connected to the sampler using a tube connecter, then both tube and bottle are wised by seawater sample for three times. Next, fill the 250ml Screw-type Durand bottle smoothly from the bottom using the drawing tube and overflow for a while. To allow for the expansion of the cold seawater as it warms, tap the bottle with a finger to remove a small amount of sample, leaving about 1% of the bottle volume as headspace. After that, take 167 $\mu\mathrm{L}$ of 50% Mercury chloride (II) solution from the 5ml Brown screw-type bottle with a pipette to poison the sample. Finally, crew the bottle cap carefully, then invert the bottle several times to disperse the mercuric chloride (II) solution thoroughly.

Table 0.2 Equipment and medicine used for water sampling.

AAQ-1183 & AAQ-177 direct reading water quality meter (JFE ADVANTEC Corporation)
RIGO-B transparent water sampler (RIGO Corporation)
250ml Screw-type Durand bottle
Silicon drawing tube & tube connector
$30\mu\text{L} \sim 300\mu\text{L}$ Eppendorf Volumetric Pipette & tips
5ml Brown screw-type bottle
50% Mercury chloride (II) solution

Mercury chloride solution is added to prevent the amount of CO2 in the sample container from changing due to biological activities such as respiration, photosynthesis, and decomposition. The Mercury chloride(II) solution is prepared in the laboratory under 20℃ conditions, to prevent Mercury chloride(II) crystals from precipitation when the temperature drops; a 50% saturated solution was used [17]. In addition, considering its characteristic of decomposition under light, brown screw-type bottles are used for storage [21].

For sample containers, reagent bottles made of borosilicate glass such as Schott Duran® are considered suitable. In this study, screw-type Duran bottles instead of sliding stopper type were used, for the fact that they are expected to meet the required accuracy [22].

Figure 2.4 Water sampling

The depth at the sampling spot can be calculated from the measured depth of the mooring system or AAQ. The depth is measured by bottom water level sensor plus 0.5m(the sensor is 0.5m from the bottom), or the deepest depth measured by AAQ plus 0.12m(depth sensor of AAQ is designed 0.12m away from bottom). While the depth calculated from these two kinds of measuring equipment is not the same, one reason might be that when we use the AAQ to measure the depth, turbidity is used as judgment criteria that the moment AAQ reaches the bottom, turbidity measured by AAQ would suddenly increase. This works in most cases, but like the situation in Feb. 4th afternoon, when seawater was severely disturbed by the wind that rising turbidity in water made it hard to judge so that we had to decide from the impact transmitted from cable. Also, the sediment on the bottom may interfere with the result of AAQ. For the above two reasons, we decide to trust the depth measured by the mooring system.

Figure 2.5 Bottom of sampling spot taken by a water-proof camera on Feb.3rd

2.4 Survey schedule

The mooring system was set in the field during the field survey(see Table 2.5), measuring water parameters at 10 min intervals. For water sampling and AAQ measuring in the vertical direction, we stayed in the field to repeat the operation once per hour in the daytime, while in the nighttime we walked from the hotel closest to the sampling spot every two hours until 1 a.m.

Table 0.3 Survey schedule

Time slots
2020 Dec 24th 13:30 - Dec 25th 17:00
2021 Feb 3rd 12:20 -Feb 4th 17:00
2021 April 26th 11:40 - April 27th 17:00
2021 June 1st 10:00 - Dec 2nd 17:00

2.5 Sample storage

The samples were stored in a plastic container in winter and cooler cases in spring during the field survey. Collected samples were immediately transported to Coastal Environment lab, GSFS, UTokyo, which were kept in a cool and dark place in the experiment room with room temperature maintained at 20℃ until measurement. The measurements were completed within 3 to 4 days after sample collection to minimize the effect of air ingress through the screw openings of the bottles.

2.6 Preparation and calibration of sensors

2.6.1 pH

In surveys in December and February, AAQ-1183 was used, while in surveys in April and June, AAQ-177 was used. With the AAQ-177, DO and pH data can be collected. Before the survey, the pH sensor of AAQ was calibrated in lab condition using pH standard solution equal to 6.86 and 9.18[23], while the HOBO pH sensor is calibrated using pH standard solution equal to 4 and 7 [24]. AAQ pH sensor, HOBO pH sensor, and ATT-05 pH sensor mentioned in section 2.2 were soaked in the same solution under lab conditions, and the pH reading of these three kinds of sensors was the same.

Due to security issues, we did not keep the AAQ in seawater during the survey but locked it in a bag when it is not used. In April, we used distilled water to clean the pH sensor after each measurement, and then insert the pH sensor into a cap filled with distilled water. Since the pH sensor needs time to get used to seawater, and the pH of distilled water is much lower than the seawater, pH measured by AAQ-177 was lower than the actual condition, especially the surface seawater was measured lower the pH 7 at some time. In June, we improved our method to use tap water to clean the pH sensor and insert the sensor into a cap filled with KCL solution. Before each measurement, we soaked the sensor in seawater for 10 to 20s. This time, pH measured by AAQ do not have inconsistency with environment condition. We use the pH data measured by HOBO in December, February, and April, as well as the pH measured by AAQ in June for analysis.

Comparing to the AAQ, the HOBO pH sensor was kept and got used to the seawater, we thereby choose to regard HOBO pH data as the accurate one.

2.6.2 DO

AAQ DO sensor was calibrated under 100% DO condition (pump air into water for 30 min to make 100% DO condition) and 0% DO condition (dissolving 5g of sodium sulfite in 100ml distilled water) [23]. HOBO DO sensors were only calibrated under a 100% DO condition by putting a wet sponge in the calibration boots and insert the DO sensor into the boots for 15 min [25].

Two HOBO DO sensors were put in the same water for a test, even though they are the same product, the measured DO values had a 0.1 mg/L difference. HOBO DO sensor is also compared with AAQ-177 DO sensor, their difference was around 0.1 to 0.2 mg/L. These discrepancies can be eliminated using field data calibration. This means using the third reliable sensor to measure DO data, then use the data at the beginning and the end of a survey to calibrate HOBO DO data. For the surveys in December and February, an LDO [fluorescent dissolved oxygen] probe (by HACH company) was used for field data calibration; in April and June, AAQ-177 DO sensor was used for field data calibration.

2.6.3 Electric Conductivity and salinity

Electric conductivity measured by sensors made by JFE ADVANTEC Corporation is usually considered accurate. Figure2.7, which plots part of the survey data as an example, compares the EC measured by AAQ and the EC measured by the HOBO EC sensor. Neither the HOBO EC raw data nor the default factory calibrated HOBO EC data matches with AAQ EC data. Even the HOBO EC field calibrated data, that use the AAQ EC data for calibration does not match with AAQ EC data. As the salinity is calculated from electric conductivity, the HOBO salinity data also does not match with AAQ salinity data. This kind of inconsistency is considered from the calibration software itself.

We decided to use the salinity measured by AAQ for analysis. Although the absolute value of electric conductivity measured by the HOBO EC sensor may not be accurate, the measured data can reflect the changing EC tendency in the field.

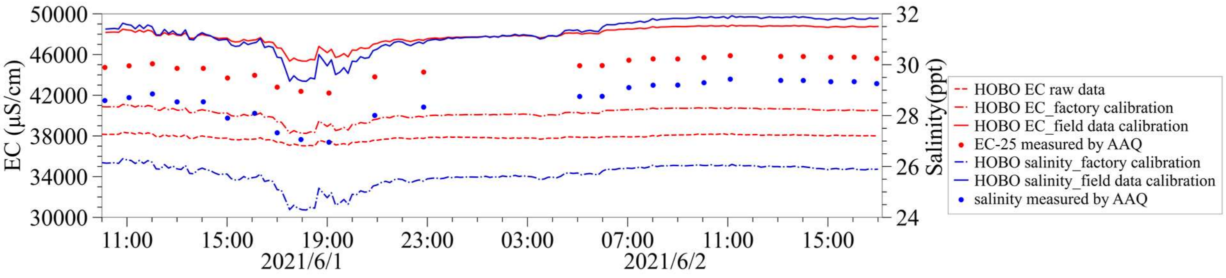

Figure 2.6 Inconsistency in AAQ and HOBO measured EC result

2.7 Analysis of $\mathbf{A_T}$ and DIC

2.7.1 ATT-05

The total alkalinity titration machine ATT-05 from Kimoto Electronics Industry Co was used to measure $\mathrm{A_T}$ and

DIC. The titration method is based on the principle of neutralization titration and can be selected from the open-cell method and the closed-cell method. For the open-cell method, ATT-05 injects the acid rapidly till degassing pH level, then it starts titration to measure total alkalinity without the influence of carbonates. For the closed-cell method, the seawater sample is titrated under the condition the carbonates exists to measure total alkalinity and total dissolved inorganic carbon at the same time [26]. In this study, the latter method was selected to measure both $\mathrm{A_T}$ and DIC to test the consistency in the measurement result.

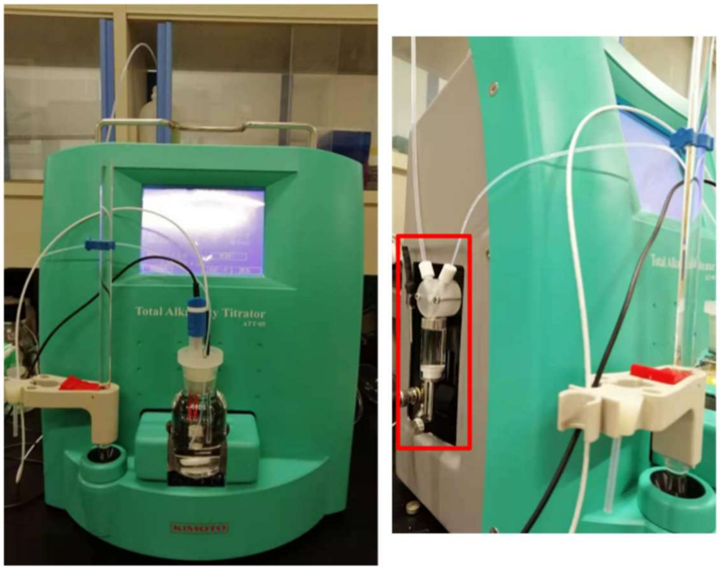

Figure 2.7 ATT-05; left: overall view, right: pumping syringe

2.7.2 Reagent

The reagents used in this experiment are listed in Table 2.4. The standard concentration of HCL solution used in the neutralization titration is 0.1 mol/L. 3.3 mol/L KCL solution is used as the internal solution of the electrode, which gradually decreases with time due to leakage into the sample. Phosphate buffer of pH 6.881 and phthalate buffer of pH 4.002 under 20℃ lab condition are used in two-point calibration. The accuracy of the experiment was checked using standard reference seawater, which is surface seawater collected from Kemigawa Beach Jetty on 2020 Nov.14th and poisoned with Mercury chloride (II) solution.

The total alkalinity value of the standard reference seawater is fixed by Mercury chloride(II) solution, and test results from 2020 November to 2021 June shows that the total alkalinity value fluctuates within the range of 2240-2244μmol/kg.

Table 0.4 Reagents used in the experiment and their usage

Reagents	Usage
0.1 mol/L HCL solution	Neutralization titration
3.3 mol/L KCL solution	Electrode internal fluid replenishment
pH Standard Solution Phosphate Buffer	pH sensor calibration
pH Standard Solution Phthalate Buffer	pH sensor calibration
Standard reference seawater	Accuracy confirmation

2.7.3 Operation procedure

1. Preparation sequence of ATT-05 is listed in Table2.5 [26].

Table 0.5 preparation sequence

①Boot	②Warming-up	③Temperature & pH calibration	④Measure data setting	⑤Stirrer setting

2.Titrating reagent installation.
3. Replenish pH sensor
4. Transfer water sample:
5. Update Measurement information and start the experiment.

In the second step of installing titrating reagents, the position of the HCL solution bottle should be placed on the shelf behind and higher than the equipment to avoid the heat from the machine to transmit to the reagent. Heat on the reagent may affect the accuracy. Also, the pumping syringe should be rinsed out 2 to 3 times before experiment by pumping in and out the HCL solution to remove the air inside. Bubbles in the syringe can cause the titration volume to vary and measured total alkalinity will be a bit higher than usual.

In step three, the remaining amount of KCL solution in the pH sensor needs to be more than 60%. If is lower than this amount, the reading of the pH sensor can be unstable.

For the fourth step, a plastic syringe connected with a silicon tube should be prepared beforehand. Rinse out this tool set with the seawater sample about to be measure, then use the rinsed tool set to transfer the water sample into a dedicated alkalinity bottle after the bubbles in the syringe is completely removed. By using the plastic syringe and tube set, contact between sample and air can be minimized.

Furthermore, some important measures are needed to be taken after the experiment as following. After pumping out the remaining HCl solution, pump in and out distilled water into the syringe three times to wash away HCL; then pump in and out air for three times to remove distilled water. HCL solution remained inside the syringe for a long time can cause the metal parts to rust.

About the storage of pH sensor, in the case of long-term storage, plug pH sensor into the cap filled with distilled water, and cover the cap with parafilm to prevent leakage; while in the case of short-term storage, simply soak the sensor in acidified seawater.

2.7.4 Measurement principle

This section refers to the Total Alkalinity Titrator ATT-05 Instruction Manual[26] of Kimoto Electronics Industry Co. The total alkalinity of a sample of sea water is defined as the number of moles of hydrogen ion equivalent to the excess of proton acceptors over proton donors in 1 kilogram of sample:

$$\begin{aligned}\mathrm{A_T} = {} & [\mathrm{HCO_3^-}] + 2[\mathrm{CO_3^{2-}}] + [\mathrm{B(OH)_4^-}] + [\mathrm{OH^-}] + [\mathrm{HPO_4^{2-}}] + 2[\mathrm{PO_4^{3-}}] \\ & + [\mathrm{SiO(OH)_3^-}] + [\mathrm{NH_3}] + [\mathrm{HS^-}] \ldots - [\mathrm{H^+}]_\mathrm{F} - [\mathrm{HSO_4^-}] - [\mathrm{HF}] \\ & - [\mathrm{H_3PO_4}] + \cdots \end{aligned} \tag{2.1}$$

where the ellipses stand for additional minor acid or base species that are either unidentified or present in such small amounts that they can be safely neglected.

At any point in the titration, the analytical total concentration of hydrogen ion (relative to this proton condition) is given by the expression:

$$\begin{aligned}\mathrm{C_H} = {} & [\mathrm{H^+}]_\mathrm{F} + [\mathrm{HSO_4^-}] + [\mathrm{HF}] + [\mathrm{H_3PO_4}] - [\mathrm{HCO_3^-}] - 2[\mathrm{CO_3^{2-}}] - [\mathrm{B(OH)_4^-}] \\ & - [\mathrm{OH^-}] - [\mathrm{HPO_4^{2-}}] - 2[\mathrm{PO_4^{3-}}] - [\mathrm{SiO(OH)_3^-}] - [\mathrm{NH_3}] - [\mathrm{HS^-}] \end{aligned} \tag{2.2}$$

At any point in the titration, after a mass m of acid with concentration C (mol kg-soln–1) has been added to a mass $\mathrm{m_0}$ of sample

$$\mathrm{C_H} = \frac{-\mathrm{m_0 A_T} + \mathrm{mC}}{\mathrm{m_0} + \mathrm{m}} \tag{2.3}$$

This can be equated to the previous expression for $\mathrm{C_H}$:

$$\begin{aligned}\frac{-\mathrm{m_0 A_T} + \mathrm{mC}}{\mathrm{m_0} + \mathrm{m}} = {} & [\mathrm{H^+}]_\mathrm{F} + [\mathrm{HSO_4^-}] + [\mathrm{HF}] + [\mathrm{H_3PO_4}] - [\mathrm{HCO_3^-}] - 2[\mathrm{CO_3^{2-}}] \\ & - [\mathrm{B(OH)_4^-}] - [\mathrm{OH^-}] - [\mathrm{HPO_4^{2-}}] - 2[\mathrm{PO_4^{3-}}] - [\mathrm{SiO(OH)_3^-}] \\ & - [\mathrm{NH_3}] - [\mathrm{HS^-}] \end{aligned} \tag{2.4}$$

This equation is the basis of all computations involved in this procedure.

The concentration of each species of ions in equation (2.4) can be substituted by the expressions in Table 2.6.

Table 0.6 Expression for the concentrations of the various species in equation (2.4)

$[\mathrm{HCO_3^-}] = \frac{\mathrm{C_T K_1 [H^+]}}{\mathrm{[H^+]^2 + K_1[H^+] + K_1K_2}}$
$[\mathrm{CO_3^{2-}}] = \frac{\mathrm{C_T K_1 K_2}}{\mathrm{[H^+]^2 + K_1[H^+] + K_1K_2}}$
$\left[\mathrm{B(OH)^-{}_4}\right] = \mathrm{B_T/(1 + [H^+]/K_B)}$
$\mathrm{[OH^-] = K_w/[H^+]}$
$\mathrm{[H_3PO_4]} = \frac{\mathrm{P_T[H^+]^3}}{\mathrm{[H^+]^3 + K_{1P}[H^+]^2 + K_{1P}K_{2P}[H^+] + K_{1P}K_{2P}K_{3P}}}$
$\mathrm{[H_2PO_4^-]} = \frac{\mathrm{P_T K_{1P}[H^+]^2}}{\mathrm{[H^+]^3 + K_{1P}[H^+]^2 + K_{1P}K_{2P}[H^+] + K_{1P}K_{2P}K_{3P}}}$
$\mathrm{[HPO_4^{2-}]} = \frac{\mathrm{P_T K_{1P}K_{2P}[H^+]}}{\mathrm{[H^+]^3 + K_{1P}[H^+]^2 + K_{1P}K_{2P}[H^+] + K_{1P}K_{2P}K_{3P}}}$
$\mathrm{[PO_4^{3-}]} = \frac{\mathrm{P_T K_{1P}K_{2P}K_{3P}}}{\mathrm{[H^+]^3 + K_{1P}[H^+]^2 + K_{1P}K_{2P}[H^+] + K_{1P}K_{2P}K_{3P}}}$
$\left[\mathrm{SiO(OH)^-{}_3}\right] = \mathrm{Si_T/(1 + [H^+]/K_{Si})}$
$\mathrm{[NH_3] = NH_{3_T}/(1 + [H^+]/K_{NH_3})}$
$\mathrm{[HS^-] = H_2S_T/(1 + [H^+]/K_{H_2S})}$
$\mathrm{[H^+]_F = [H^+]/(1 + S_T/K_S)}$
$\mathrm{[HSO_4^-] = S_T/(1 + K_S/[H^+]_F)}$
$\mathrm{[HF] = F_T/(1 + K_F/[H^+])}$

Each term in the form of $\mathrm{X_T}$ denotes the total dissolved inorganic X. All the listed $\mathrm{X_T}$ terms are summarized in Table 2.7 in the form of mass-conservation equations.

In this section, the expressions of the components in a solution are unified as $\mathrm{X_T}$, among which $\mathrm{C_T}$ is the same as DIC.

Table 0.7 Mass-conservation equations

$\mathrm{C_T = [CO_2^*] + [HCO_3^-] + [CO_3^{2-}]}$
$\mathrm{B_T = [B(OH_3)] + [B(OH)_4{}^-]}$

$S_T = [HSO_4^-] + [SO_4^{2-}]$
$F_T = [HF] + [F^-]$
$P_T = [H_3PO_4] + [H_2PO_4^-] + [HPO_4^{2-}] + [PO_4^{3-}]$
$Si_T = [Si(OH)_4] + [SiO(OH)^-{}_3]$
$NH_{3_T} = [NH_4^+] + [NH_3]$
$H_2S_T = [H_2S] + [HS^-]$

The K terms in Table 2.6 refer to equilibrium constants defined in Table 2.8.

Table 0.8 Equilibrium constants

$K_0 = [CO_2^*]/f(CO_2)$
$K_1 = [H^+][HCO_3^-]/[CO_2^*]$
$K_2 = [H^+][CO_3^{2-}]/[HCO_3^-]$
$K_B = [H^+]\left[B(OH)^-{}_4\right]/[B(OH_3)]$
$K_w = [H^+][OH^-]$
$K_S = [H^+][SO_4^{2-}]/[HSO_4^-]$
$K_F = [H^+][F^-]/[HF]$
$K_{1P} = [H^+][H_2PO_4^-]/[H_3PO_4]$
$K_{2P} = [H^+][HPO_4^{2-}]/[H_2PO_4^-]$
$K_{3P} = [H^+][PO_4^{3-}]/[HPO_4^{2-}]$
$K_{Si} = [H^+]\left[SiO(OH)^-{}_3\right]/[Si(OH)_4]$
$K_{NH_3} = [H^+][NH_3]/[NH_4^+]$
$K_{H_2S} = [H^+][HS^-]/[H_2S]$

Equation (2.2) is used together with the ideal Nernst equation:

$$E = E^0 - \left(\frac{RT}{F}\right) \ln\, [H^+] \tag{2.5}$$

Here, E is pH electrode potential (mV), E^0 is Standard oxidation-reduction potential (mV),
R is gas constant (J/K/mol), F is Faraday constant (C/mol).
By changing the formation of equation (2.5), values of $[H^+]$ are computed from an initial estimate of E°:

$$[H^+] = \exp\left(\frac{E - E^\circ}{RT/F}\right) \tag{2.6}$$

Equation (2.4) can be rewritten as equation (2.7), terms with a negligible contribution to A_T has already been deleted from the original equation.

$$A_T = C_T\left(\frac{K_1[H^+] + 2K_1K_2}{[H^+]^2 + K_1[H^+] + K_1K_2}\right) + B_T\left(\frac{1}{1 + [H^+]/K_B}\right) - S_T\left(\frac{1}{1 + K_s(1 + S_T/K_s)/[H^+]}\right) - F_T\left(\frac{1}{1 + K_F/[H^+]}\right) - \left(\frac{m_0 + m}{m_0}\right)\left(\frac{[H^+]}{(S_T + 1)/K_s} - \frac{K_w}{[H^+]}\right) + \frac{m}{m_0}C \tag{2.7}$$

For the open-cell method, C_T in equation (2.7) is assumed to be zero since $[HCO3^-]$ and $[CO3^{2-}]$ are degassed as CO2 by injection of acid. After degassing is completed, the potential of the pH electrode varies with the dispensing amount of HCl solution. A_T is calculated in the range from pH 3.5 to 3.0 by using equation (2.7), and A_T is assumed to show the constant value within this range. Electrode E^0 with minimum deviation is determined using dozens of A_T points contained in this range of pH by non-linear least-square technique.

While, for the closed-cell method which we use in this study, C_T is not zero as dissolved CO2 exists in the higher pH region. Therefore, for all effective titration points, the A_T and C_T are calculated by optimizing the result of the equation (2.9) and the equation (2.8).

$$X = C_T\left(\frac{K_1[H^+] + 2K_1K_2}{[H^+]^2 + K_1[H^+] + K_1K_2}\right) \tag{2.8}$$

$$Y = B_T\left(\frac{1}{1 + [H^+]/K_B}\right) - S_T\left(\frac{1}{1 + K_s(1 + S_T/K_s)/[H^+]}\right) - F_T\left(\frac{1}{1 + K_F/[H^+]}\right) - \left(\frac{m_0 + m}{m_0}\right)\left(\frac{[H^+]}{(S_T + 1)/K_s} - \frac{K_w}{[H^+]}\right) + \frac{m}{m_0}C \tag{2.9}$$

The deviation is assumed to be constant for the dispensed volume of HCl solution when it compared the variation of A_T with the variation of C_T. Then electrode $E°$ and K1 factor are determined by a non-linear least-square technique that approaches to r^2=1 of linear expression. Finally, C_T and A_T are computed by using slope value and intercept value on the X-Y plotting graph.

2.7.5 Reliability of experiment result

For reliability of A_T, as mentioned in section 2.2.2, the total alkalinity value of the standard reference seawater tested by ATT-05 is between 2240-2244 $\mu\mathrm{mol/kg}$; and this result did not change during the half-year period. This reflects the high reproducibility of the measuring method. Before experiments, test with standard reference seawater was operated to make sure the equipment especially the pH sensor is in a good state, only when the $\mathrm{A_T}$ result of standard reference seawater falls within the above range, will the sample analysis begin. For reliability of DIC. Due to the measurement principle, when $\mathrm{A_T}$ is accurately measured, DIC is assumed to be accurate as well. However, unlike $\mathrm{A_T}$ that is not affected by CO2 exchange, DIC can be influenced. Following the operation procedure in section 2.2.3, contact between water sample and air has already been reduced to the minimum. So, the concern about the DIC result reliability is to which extend it could be influenced in the step transferring water sample from sampler to Duran bottles. Comparison on different sample-transfer methods is implemented as in Figure 2.9.

Using method (a), by leaning the short tube on the edge of the sampling bottle, bubbles can be avoided, but the water sample is exposed to air. In method (b), the long tube can reach the bottom of the sampling bottle but connecting the tube to (a) after each time's sampling caused uncertainty. Sometimes the tube is fulfilled with water, but other times, bubbles are observed in the tube. Method (c) can completely get rid of bubbles. Since the tube in (c) is thinner than the tube in (b), during transferring step, we first completely open the switch on the sampler to remove the air in the tube and then pinch the tube with fingers to control the flow rate.

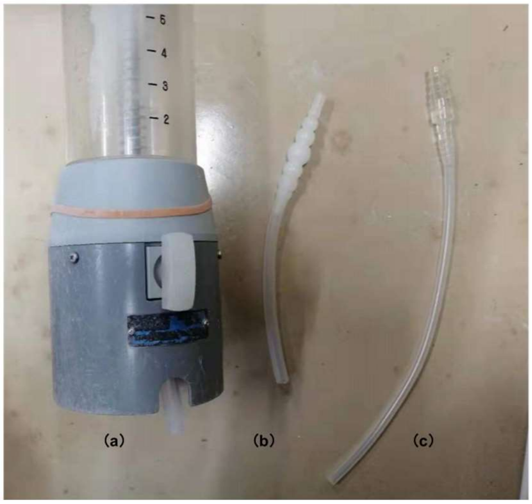

Figure 2.8 sample-transfer methods.

(a)using only the short tube connected to sampler; (b)connect the long tube with a connector in (b) to (a) after each time's sampling then transfer sample; (c)keep the long tube and connector in (c) connected to (a) even during water sampling, the long tube can be fixed to the sampler with the orange rubber band.

On 2020 November.14th, the difference between sample-transfer method (a) and sample-transfer method(b) was first checked during a survey in Kemigawa Beach. Samples were taken at the surface, middle, and bottom layers, then the water sample in the sampler (1.3 L volume) was transferred to a first bottle(250ml) with method(a), and subsequently transferred to a second bottle(250ml) with method(b) following sampling method in section 2.1.3. The difference in DIC was 2-4 $\mu\mathrm{mol/kg}$ for the same seawater in sampler transferred by different methods, see Figure 2.10.

By the way, the 250ml volume of Duran bottle offers us a chance to measure the same sample twice, and the DIC difference of two continuous experiments for the same sample was 0.2 to 3 $\mu\mathrm{mol/kg}$. Besides, the pressure change due to the opening of the screw-type Duran bottle is supposed to affect the second-time experiment.

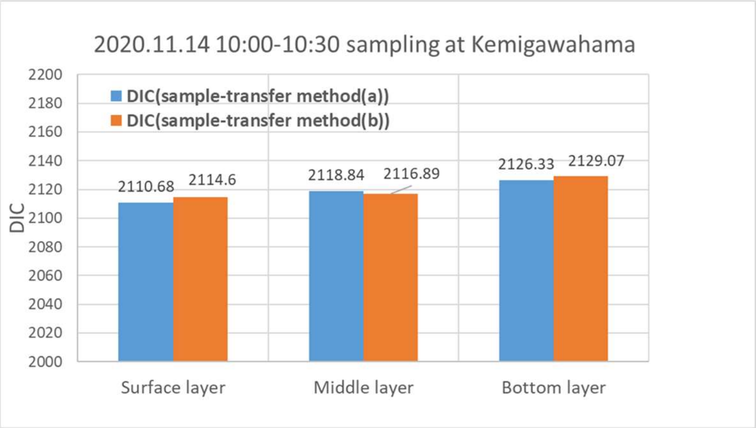

Figure 2.9 Comparison of sample-transfer method (a) and (b)

Sample-transfer method(b) was used in surveys in December, February, and April, but there are several times bubbles were observed in the long tube, we thereby applied the method(c). The difference caused by method(b) and method(c) was tested in lab condition with artificial seawater. Artificial seawater with different salinity was prepared and sampled with the same procedure in section 2.1.3, just as the comparison work operated at Kemigawa Beach, same water in the sampler was transferred first with method(b), next with method(c). Because of the uncertainty of method(b), there were times when the result was identical, while the other time, the difference can be as large as 2.6 $\mu\mathrm{mol/kg}$. Moreover, it was better to regard the test result with artificial seawater as a qualitative one that the difference caused by the different sample-transfer methods is very small, rather than a quantitative one, because the DIC of artificial seawater is far larger than the recommended measurement range.

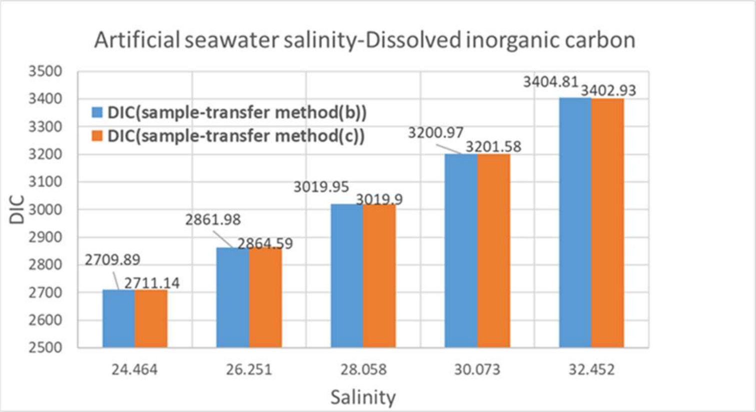

Figure 2.10 Comparison of sample-transfer method (b) and (c)

In addition, the maximum relative standard deviation of DIC using ATT-05 is reported to be 0.20%[26]. By applying the equation (2.11) inversely, the standard deviation for the seawater taken at Kemigawa Beach can be calculated to be 4.2 $\mu\mathrm{mol/kg}$. For the reason the measured DIC difference is within the standard deviation, a conclusion can be drawn that the error of DIC caused in the sampling step is within the acceptable range.

$$s = \sqrt{\frac{\sum(x-\bar{x})^2}{n-1}} \tag{2.10}$$

$$\mathrm{RSD} = \frac{s}{x} \tag{2.11}$$

2.8 $\mathbf{pCO_{2sw}}$ Calculation

2.8.1 CO2SYS

CO2SYS is a family of software programs applied widely by marine scientists that use any two of the inorganic carbon system parameters to calculate various chemical properties of the system, basing on the well-known thermodynamic equilibria. On the basis of a comparison result of ten publicly available software packages[27], up-to-date software with the set of constants recommended for best practices[17] is advocated for users.

In this study, the most recent version of CO2SYS -- PyCO2SYS v1.7[15], a fully functional and rigorously validated tool available for Python is adopted. PyCO2SYS was originally based on CO2SYS for MATLAB, version 2.0.5; nevertheless comparing to the old versions of CO2SYS for MATLAB, PyCO2SYS includes additional validation of all the buffer factors except for the Revelle factor, all properties associated with $\mathrm{NH_3}$ and $\mathrm{H_2S}$, and total calcium molinity[28], thus considered more robust.

For reproducibility, all chosen parameter settings are listed as follows:

Table 0.9 Parameters setting for PyCO2SYS

pH scale	Total scale
carbonic acid dissociation equilibrium constant	Lueker et al. (2000) [29]
bisulfate ion dissociation equilibrium constant	Dickson (1990) *J. Chem. Thermodyn.* [30]
boron: salinity relationship	Uppström (1974) Deep-Sea Res. [31]
hydrogen fluoride dissociation equilibrium constant	Perez & Fraga (1987) Mar. Chem. [32]
buffer factors calculation	“auto”(recommended)
gas constant (*R*)	2018 CODATA [33]

Moreover, the carbonic acid dissociation equilibrium constant in Table 2.9 is applied for the salinity range from 19 to 43 ppt, so the sample collected upstream of the East water gate with a salinity of 2.35 ppt is lower than the salinity range. In the case of river water samples(salinity lower than 19), the carbonic acid dissociation equilibrium constant is set to be Cai & Wang (1998) [34], which is used for real estuarine seawater with salinity range from 0 to 40 ppt. The pH scale is chosen to be NBS (National Bureau of Standard) scale.

$$\mathrm{pH_{NBS}} \approx -\log \mathrm{aH} = -\log\left\{[\mathrm{H^+}] \cdot [\text{Activity coefficient}]\right\} \qquad (2.12)$$

2.8.2 Calculation principle

At least two of the marine carbonate system parameters, including DIC, $\mathrm{A_T}$, pH, seawater CO2 fugacity ($f(\mathrm{CO_2})$; or its partial pressure $\mathrm{pCO_{2sw}}$, or its dry-air mole fraction xCO2), are needed to calculate the remaining parameters and solve the equilibrium state of seawater.
Equation (2.1) can be rewritten as equation (2.12):

$$\mathrm{A_T = A_W + A_C + A_B + A_P + A_{Si} + A_{NH_3} + A_{H_2S} + A_{SO_4} + A_F + A_\alpha + A_\beta} \qquad (2.13)$$

All the individual alkalinity components ($\mathrm{A_X}$) are given in the subsequent Table 2.10 in terms of independent total substance contents ($\mathrm{T_x}$) and $[\mathrm{H^+}]$, by combing information given in Table 2.6, Table 2.7, and Table 2.8.

Table 0.10 Individual alkalinity Components

$A_W = \frac{K_W}{[H^+]} - [H^+]$
$A_C = [HCO_3^-] + 2[CO_3^{2-}] = \frac{K_1 T_C([H^+] + 2K_2)}{K_1K_2 + K_1[H^+] + [H^+]^2}$
$A_B = [B(OH)_4^-] = \frac{T_B K_B}{K_B + [H^+]}$
$A_P = [HPO_4^{2-}] + 2[PO_4^{3-}] - [H_3PO_4] = \frac{T_P(K_{P1}K_{P2}[H^+] + 2K_{P1}K_{P2}K_{P3} - [H^+]^3)}{K_{P1}K_{P2}K_{P3} + K_{P1}K_{P2}[H^+] + K_{P1}[H^+]^2 + [H^+]^3}$
$A_{Si} = [H_3SiO_4^-] = \frac{T_{Si}K_{Si}}{K_{si} + [H^+]}$
$A_{NH_3} = [NH_3] = \frac{T_{NH_3}K_{NH_3}}{K_{NH_3} + [H^+]}$
$A_{H_2S} = [HS^-] = \frac{T_{H_2S}K_{H_2S}}{K_{H_2S} + [H^+]}$
$A_{SO_4} = -[HSO_4^-] = \frac{-T_{SO_4}}{1 + K_{SO_4}/[H^+]}$
$A_F = -[HF] = \frac{-T_F}{1 + K_F/[H^+]}$
$A_\alpha = \begin{cases} -[H\alpha] & \text{for} \quad -\log_{10}(K_\alpha) \le 4.5 \\ +[\alpha^-] & \text{for} \quad -\log_{10}(K_\alpha) > 4.5 \end{cases}$

The reactions and equations for the second additional component β and its alkalinity contribution A_β are identical to α given above.

In the case of DIC(T_C) and A_T are known, first, pH is determined by solving the critical alkalinity-pH equation for marine carbonate system modeling -- equation (2.12). The Newton-Raphson method is applied to equation (2.13).

$$pH_{n+1} = pH_n - \frac{A_T(pH_n, \vartheta)}{A_T'(pH_n, \vartheta)} \tag{2.14}$$

Here, the $A_T' = dA_T/dpH$, and ϑ can be any of T_C, $f(CO_2)$, $[HCO_3^-]$ or $[CO_3^{2-}]$.
Then pCO_{2sw} can be determined by equation (2.14) from T_C and pH.

$$\mathrm{pCO_{2sw}} = \frac{\mathrm{T_C[H^+]^2}}{\mathrm{K_0([H^+]^2 + K_1[H^+] + K_1K_2)}} \tag{2.15}$$

In the case that $\mathrm{A_T}$ and pH are known, first, we can determine $\mathrm{A_C}$ from $\mathrm{A_T}$ and pH using equation (2.12). DIC is then calculated from $\mathrm{A_C}$ as in equation (2.15):

$$\mathrm{DIC} \ = \frac{\mathrm{A_C(K_1K_2 + K_1[H^+] + [H^+]^2)}}{\mathrm{K_1([H^+] + 2K_2)}} \tag{2.16}$$

When DIC($\mathrm{T_C}$) and pH are known, $\mathrm{A_T}$ is calculated from $\mathrm{T_C}$ and pH using equation (2.12). $\mathrm{pCO_{2sw}}$ is then calculated from $\mathrm{T_C}$ and pH using equation (2.14).

2.8.3 Consistency in $\mathrm{pCO_{2sw}}$ calculation results

The internal consistency of PyCO2SYS has already been tested in the "round-robin" test, meaning that first determine all the variables from one given input pair, then solve the system again from the results using every possible combination as the input. All the possible pairs of total alkalinity ($\mathrm{A_T}$), dissolved inorganic carbon (DIC), pH, $\mathrm{pCO_{2sw}}$, bicarbonate ion molinity ($\mathrm{[HCO_3^-\ ]}$), and carbonate ion molinity ($\mathrm{[CO_3^{2-}\ ]}$) are inputted, resulting in the fact that the difference arising from using different input pair combinations for the same composition is ten orders of magnitude smaller than the accuracy with which these variables can be measured. [28]

Theoretically, $\mathrm{pCO_{2sw}}$ calculated from measured $\mathrm{A_T}$, DIC and pH (in the lab) for a sample should be equal, nevertheless, the calculation result for all 184 samples in this study was inconsistent with the theoretical result, as in Figure 2.5. Owing to the reason that the inconsistency is not from the calculation process itself, the measurement error is doubted. From Figure 2.12, pH is clearly influencing underestimating the $\mathrm{pCO_{2sw}}$ result.

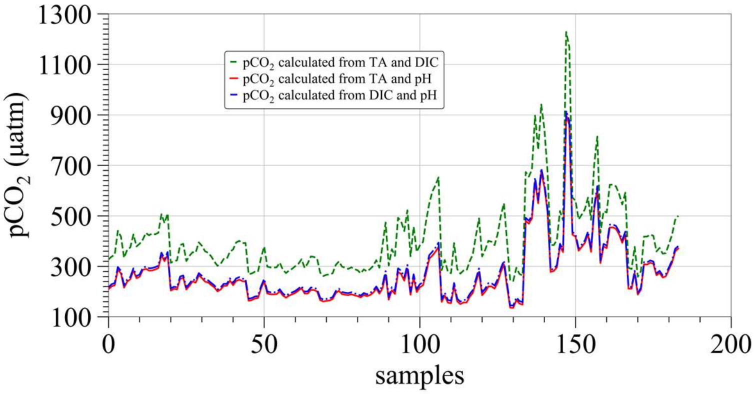

Figure 2.11 Inconsistency in $\mathbf{pCO_{2sw}}$ calculation result with direct reading pH

pH is measured under the condition that the pH electrode is calibrated, and the reading is stable. After soaking the electrode in the sample for 5 mins with the stirrer rotating, pH data is recorded. However, the standard oxidation-reduction potential E^0 used to calculate pH is not determined by measuring with a standard solution in the calibration step but obtained after optimizing the results of each time's measurements, mentioned in section 2.2.4. Therefore, instead of using the directly read result of the pH electrode before the experiment, the optimized E^0 was used to calculate pH using the equation (2.16)[26].

$$[\mathrm{H}^+] = [(\mathrm{mV} - \mathrm{E0}) / 1000 / (8.314472 * \mathrm{Temp} / 96485.3399)] \qquad (2.17)$$

$\mathrm{pCO_{2sw}}$ was calculated again using this recalculated pH, and this time, the calculated $\mathrm{pCO_{2sw}}$ is consistent with each other. Still, there is a minor difference that exists, which is supposed from the error in DIC due to contact with air. In Figure2.13, $\mathrm{pCO_{2sw}}$ calculated with $\mathrm{A_T}$ and DIC is smaller, and the $\mathrm{pCO_{2sw}}$ calculated from DIC and pH is 0.55 to 5.88 $\mu\mathrm{atm}$ smaller than the $\mathrm{pCO_{2sw}}$ calculated from $\mathrm{A_T}$ and pH, so the error in DIC caused underestimation of $\mathrm{pCO_{2sw}}$.

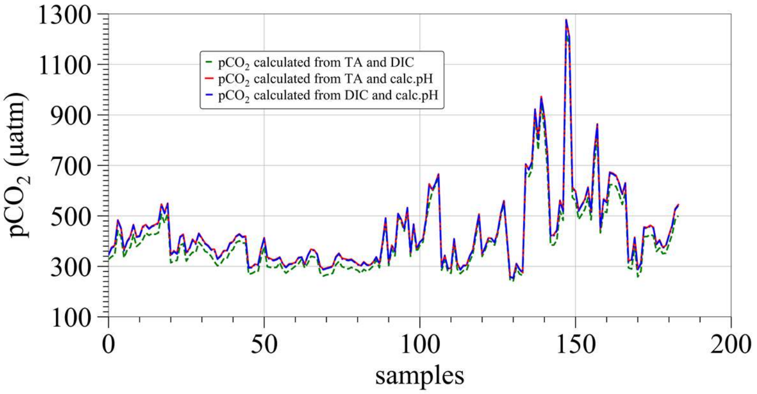

Figure 2.12 Consistent $\mathbf{pCO_{2sw}}$ calculation result with recalculated pH

With the above discussion, in this study, recalculated pH and measured A_T is adopted to calculate pCO_{2sw}.

Chapter 3 Results and Discussion

Mentioned before the head, for the scale of graphs in this section:
The scale of the graphs for water parameters is set to be the same so that it would be easy for comparison. As exceptions, scales for AAQ temperature salinity, and *chlorophyll-a* data are not completely the same. The salinity in June's survey was affected by rainfall that the salinity range was much large than other months, so only the salinity range in June was set to be 20-32 ppt to make the time-series change clearer. Also, temperature, it is so different from month to month that the temperature range is set to be 9-14℃, 14-20℃, and 20-26℃. *Chlorophyll-a* concentration in June is much higher than the other month, so it was set to be 0-25 µg/L, larger than the range in other months.

3.1 Sakai river survey on June 2nd noon

3.1.1 River Survey result

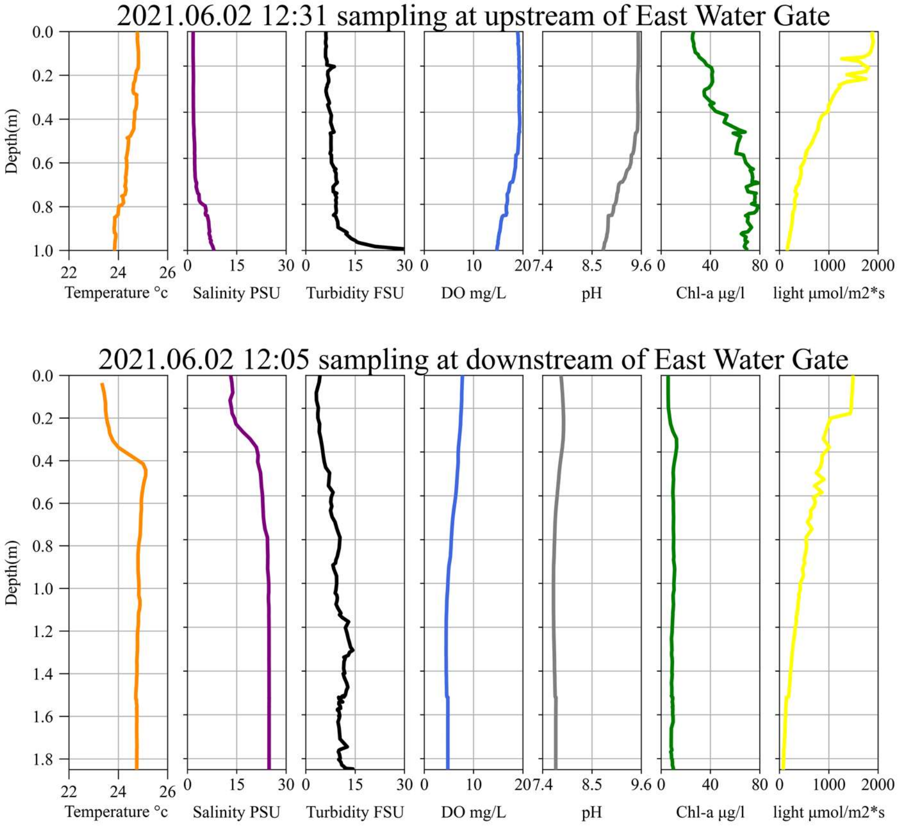

Figure 3.1 Water quality measured at upstream and downstream of East water gate with AAQ

Time-series sampling at Urayasu reveals that the sampling spot is largely influenced by the river water inflow that in order to clarify the condition of river water, we add one additional river survey during the fieldwork in June. Results in Figure 3.1 show a clear salinity gradient upstream and downstream of the watergate. Upstream of the water gate is river water, while the salinity downstream of the watergate (13-25 ppt) is very similar to the continuous sampling spot (26-29 ppt). During the low tide period, if the east watergate was open, salinity at the continuous sampling spot will be much lower. The temperature and salinity at the surface of the downstream watergate are lower than the bottom, which is supposed to be influenced by the rainwater drainage pump station located just the downstream of east watergate.

At the noon of June.2nd, much more phytoplankton exists the upstream of east water gate than downstream, strong photosynthesis by phytoplankton consumes carbonic acids in the river water, leading to much higher DO concentration and pH value in the upstream than downstream.

3.1.2 Experiment and calculation result for river water samples

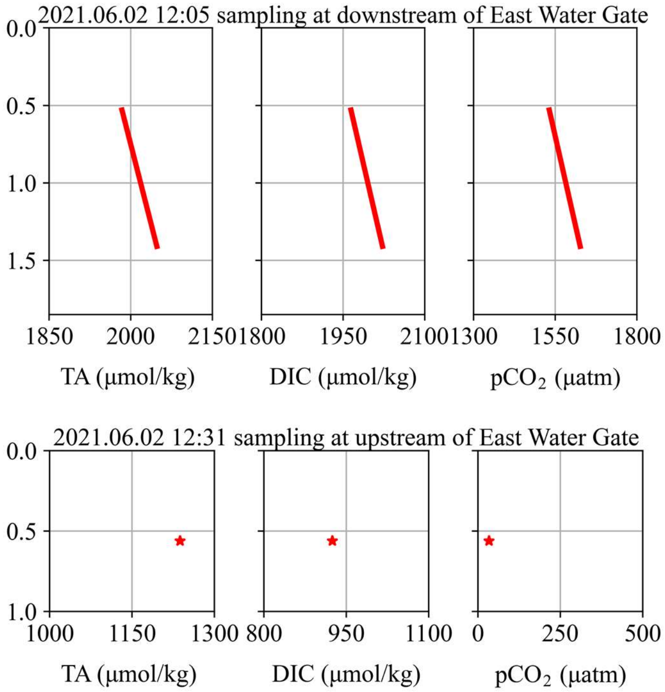

Figure 3.2 Experiment $\mathbf{A_T}$, DIC results, and calculated $\mathbf{pCO_{2sw}}$ results for water samples collected at upstream and downstream of the East watergate.

(Salinity of the upstream river water sample is lower than the recommended measuring range of ATT-05, so we only interpret the meaning of $\mathbf{A_T}$, DIC and $\mathbf{pCO_{2sw}}$ in upstream as much lower than the downstream.)

Table 0.1 Seawater carbonate system measured before and after river survey at Urayasu.

	A_T (μmol/kg)	DIC (μmol/kg)	pCO_{2sw}(μatm)
Surface (11:12)	1928.68	1782.23	565.55
Surface (13:12)	1998.4	1854.42	613.61
Bottom (11:06)	2088.55	1857.72	374.95
Bottom (13:07)	2089.43	1859.83	382.72

A_T is mentioned to be proportional to salinity, due to the low salinity in the upstream, A_T in the upstream is also very low. And because of the strong photosynthesis in the upstream, DIC and pCO_{2sw} tends to be much lower. Comparing the river sample carbonate system parameters in Figure 3.2 and the data at Urayasu before and after the river survey, when the east watergate is closed, A_T at the downstream of watergate (1984-2048 μmol/kg) is close to the A_T at continuous sampling spot, but the river water inflow may cause the A_T at least in the surface water of the continuous sampling spot to be a bit higher. The DIC (1965-2023 μmol/kg) and pCO_{2sw} (more than 1000μatm) at downstream of east watergate is higher than the DIC and pCO_{2sw} at the continuous sampling spot, river inflow may cause these two terms to be higher at the continuous sampling spot.

However, when the east watergate is open, all these three carbonate parameters will become lower at the continuous sampling spot.

3.2 Time series sampling in 2020 December

3.2.1 Survey result in December

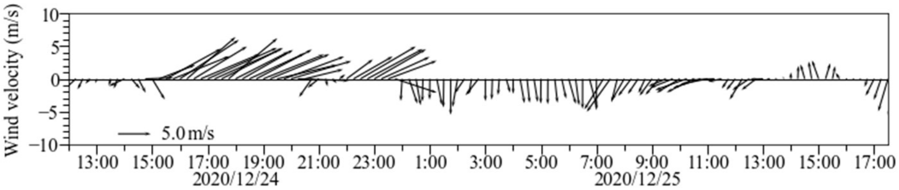

Figure 3.3 Wind measured at monitoring station during the survey in December

According to the data plotted in Figure 3.4 and Figure 3.5, water temperature change at the sampling spot during this time's survey is quite small, and the river water temperature is a bit lower than seawater, so during the low tide, the temperature at the sampling spot became smaller due to river water inflow. Similarly, EC data captured by the mooring system is observed to be steady, and the difference between the surface and bottom layer is very small, but during low tide, salinity at the sampling spot tends to be smaller because of the river water inflow. From the early morning of Dec.25th, EC difference in the surface and bottom layer of the survey spot becomes clear, this difference is thought to be caused by north wind in the Dec.25th morning that brought more river water into the sight making surface EC lower. North wind together with the low tide made this difference continuous.

Also, comparing DO and pH data at the bottom and surface layer, DO was around the oversaturated state, and the bottom DO concentration is always higher than the surface layer. After Dec.25th morning, the DO difference between surface and bottom was larger, so the river water is thought to have lower DO than seawater at the sampling location. pH changed during low tide when river water inflow to make it at both surface and bottom layer to be smaller, but the difference of pH between surface and the bottom layer was not clear until December morning due to the same reason as other water parameters.

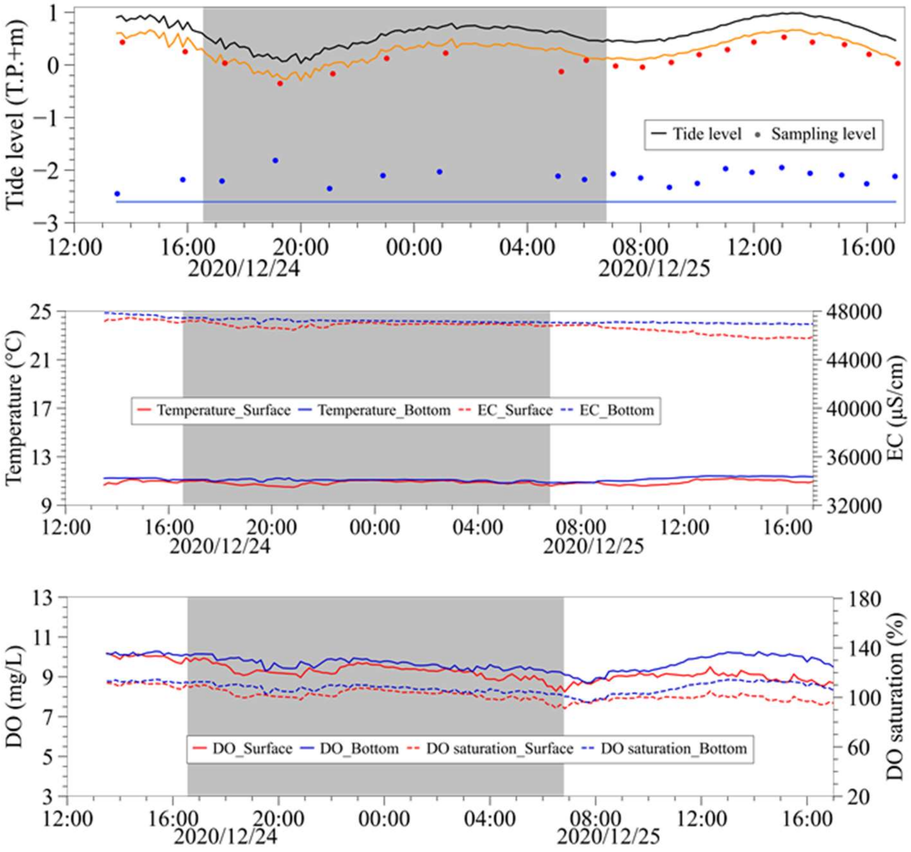

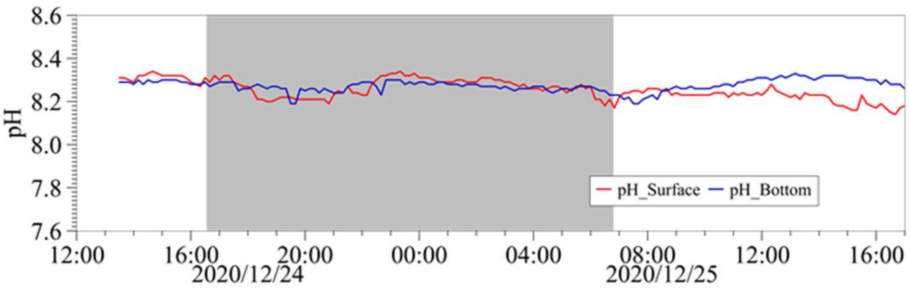

Figure 3.4 Tide level, Temperature, EC, DO, pH data captured by mooring system in December

In the graph plotting the tide level, the blue line is the water level measured by the bottom sensor, and the orange line is the water level measured by the surface sensor.

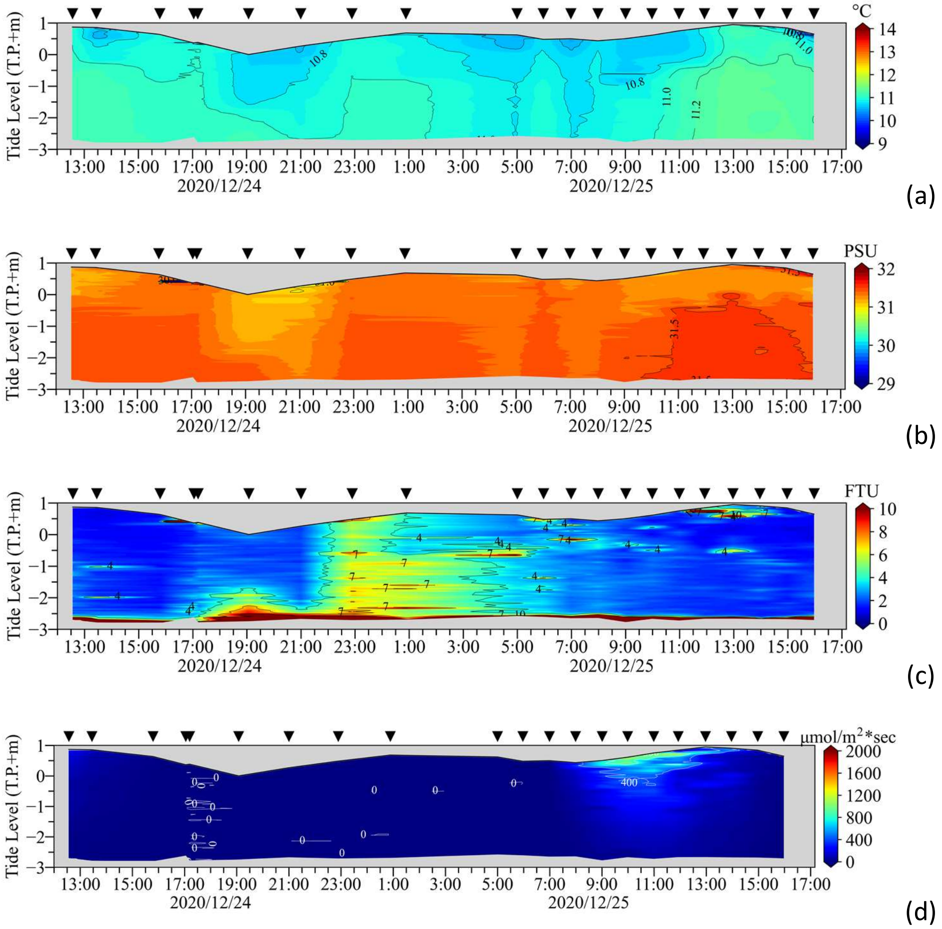

(a)

(b)

(c)

(d)

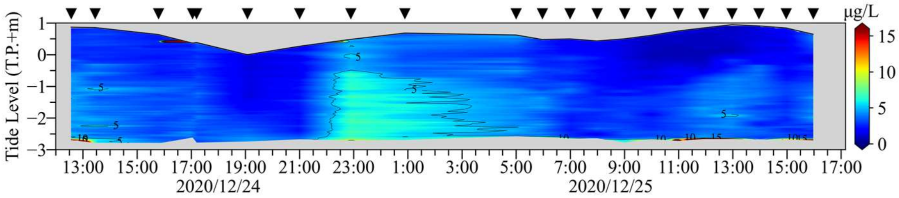

(e)

Figure 3.5 AAQ Water parameter data in December. (a)Temperature, (b)Salinity, (c)Turbidity, (d)Light quantum, (e)*Chlorophyll-a* concentration

From Figure3.5, *chlorophyll-a* concentration in the water was very low during this time's survey indicating the existence of phytoplankton in the seawater is very little, and turbidity is small except in the bottom layer due to the sediments. On Dec.24th night, a water body containing higher turbidity and *chlorophyll-a* is thought to be moved to this monitoring sight by the southwest wind. The weather was cloudy during the survey, so the light quantum in the seawater is comparatively low.

3.2.2 Experiment and calculation result in December

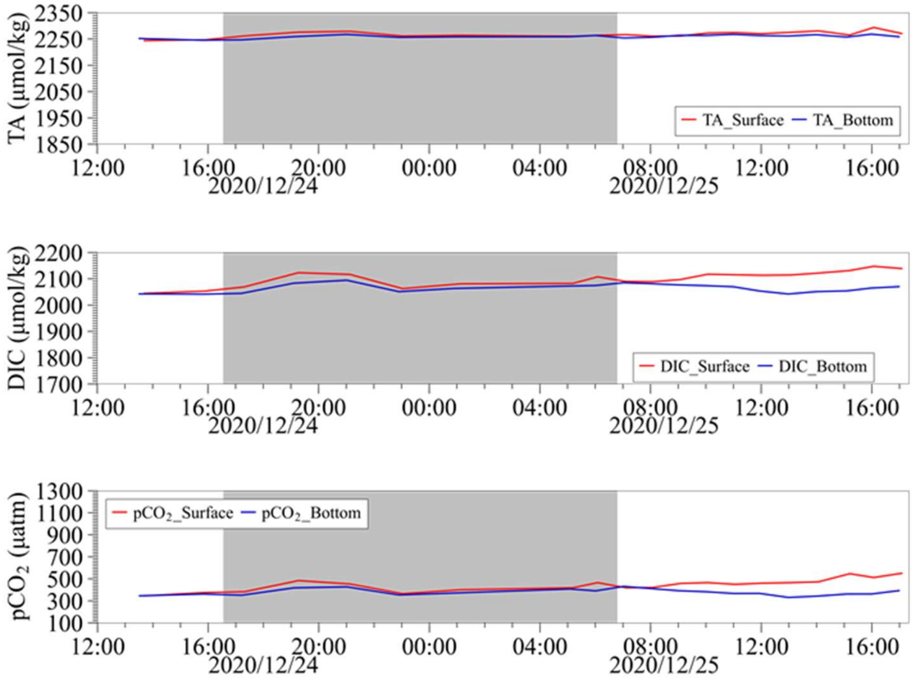

Figure 3.6 Experiment A_T , DIC results, and calculated pCO_{2sw} results for water samples collected in December

The survey in December captures complete no bloom condition, so we observed how the water exchange influenced the carbonate system at this location. Generally, the change in the carbonate system is very small.

The range of A_T is between 2240 to 2300 $\mu mol/kg$, DIC in the range from 2040 to 2150 $\mu mol/kg$, and pCO_{2sw} is from 310 to 510 μatm. During the low tide and a north wind blowing, all these three terms became higher in both surface and bottom layer due to river water inflow. And the surface layer is more influenced by river water than the bottom layer.

3.3 Time series sampling in 2021 February

3.3.1 Survey result in February

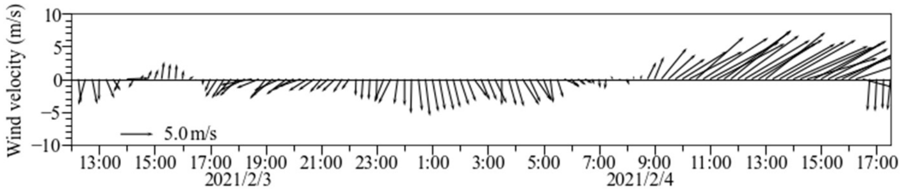

Figure 3.7 Wind measured at monitoring station during the survey in February

In Figure 3.7, the wind direction changed from north to south on Feb.4th afternoon, and this strong south wind is reported to be “Haruichiban”.

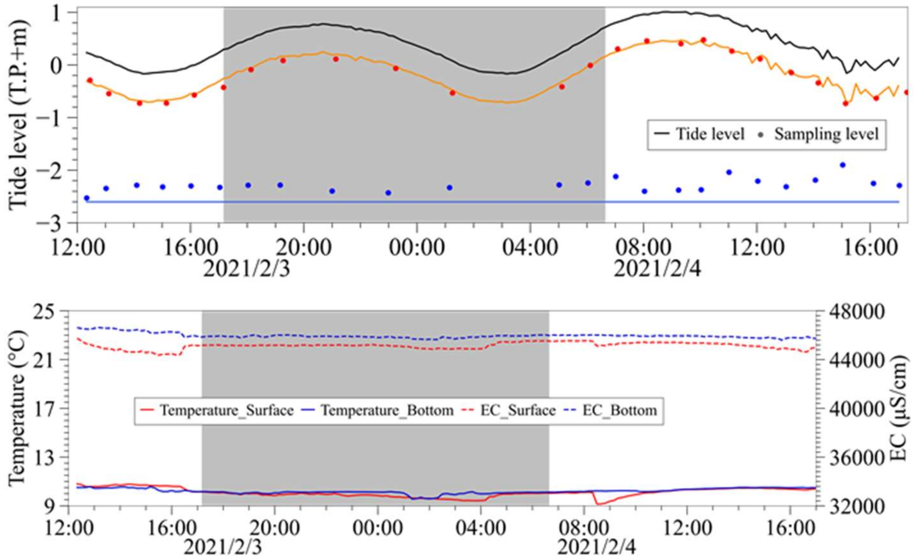

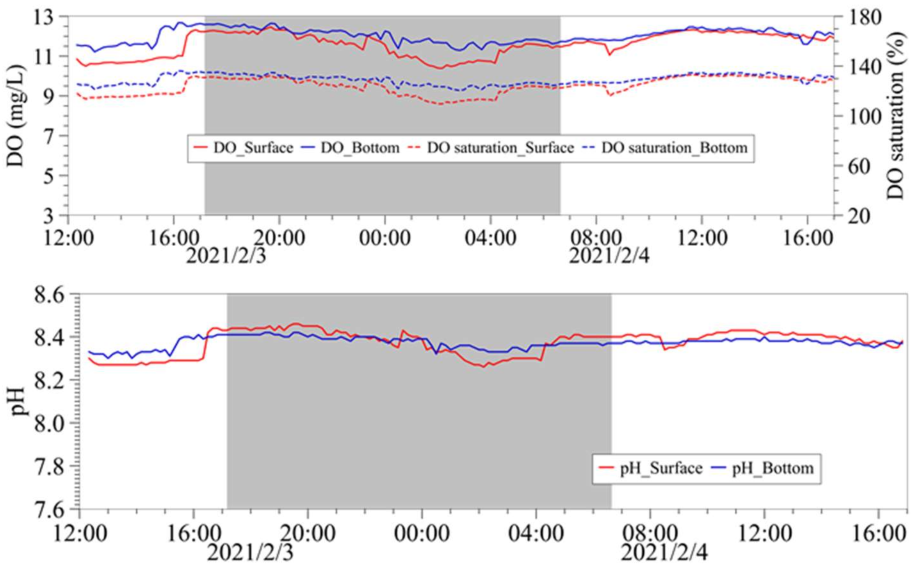

Figure 3.8 Tide level, Temperature, EC, DO, pH data captured by mooring system in February

Similar to the case in December, the temperature difference in the surface and bottom is very close in February, but during the low tide, the surface temperature became higher than the bottom in Fev.3rd h afternoon, while became equal to bottom in the early morning and afternoon of 2.4th, showing that different from December, river water temperature is equal to or larger than the seawater temperature in February. Salinity gradient can be seen

from Feb.3rd afternoon to Feb. 4th morning, and appeared again in Feb.4th afternoon, matching with the low tide and north wind period. Compared to Figure 3.9, in Figure 3.8 difference in EC can always be seen in the bottom and surface, but the difference became smaller on Feb.4th morning when the north wind stopped in the high tide period.

In this time's survey, DO is completely oversaturated in the seawater, still DO becomes lower during low tide as in December. pH, on the one hand, follows the change of tide level that drops during low tide, on the other hand, during the high tide period, surface pH is clearly larger than the bottom layer, indicating that photosynthesis may happen in the surface layer to some extent.

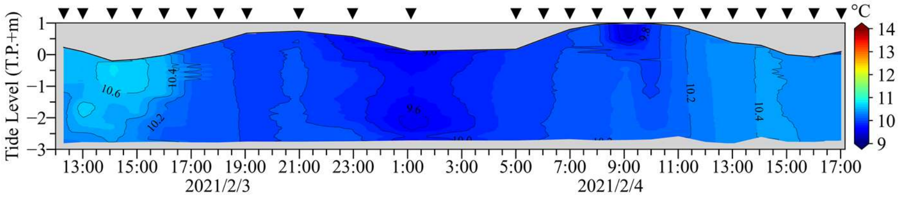

(a)

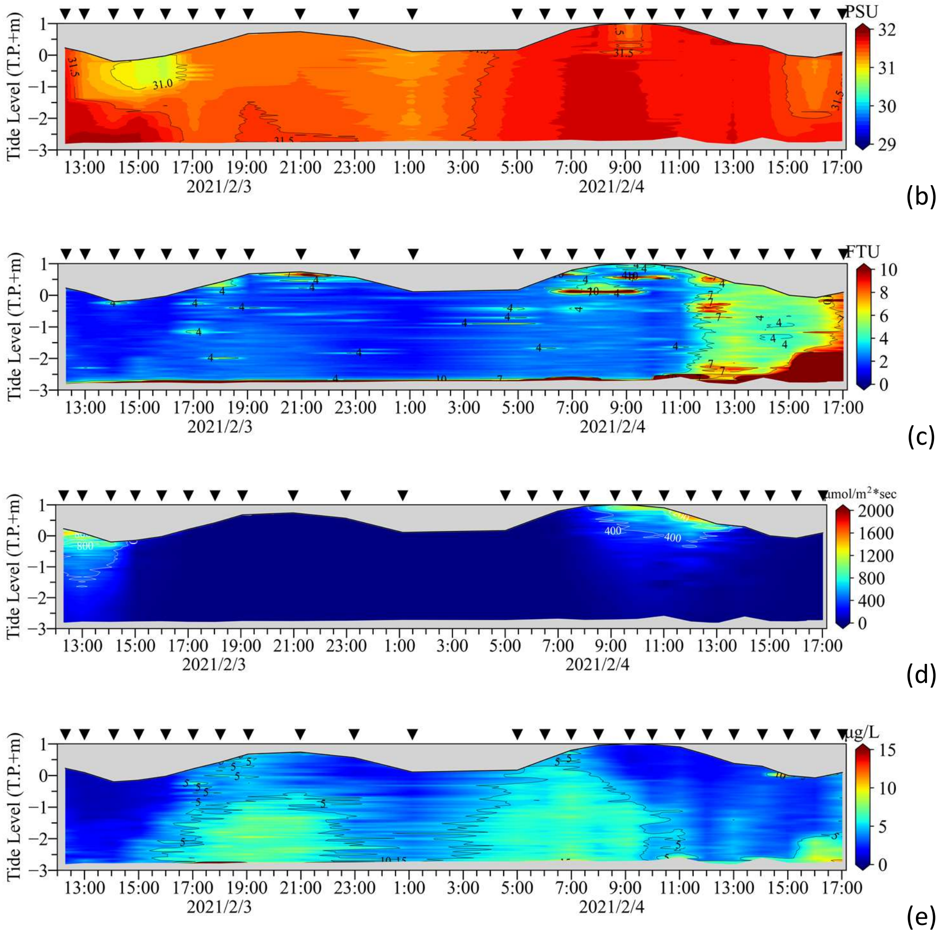

Figure 3.9 AAQ Water parameter data in February. (a)Temperature, (b)Salinity, (c)Turbidity, (d)Light quantum, (e)*Chlorophyll-a* concentration

Because of the strong south wind on Feb.4th afternoon, the seawater was disturbed that turbidity rose in the water column as in Figure3.9 (c), and in Figure 3.9(d) along with Figure 3.9(e), both light quantum and *chlorophyll-a* concentration in water was higher than December. According to the information from the Urayasu monitoring station, this time's survey was operated just before the phytoplankton blooms, which supports the guess that photosynthesis happened.

3.3.2 Experiment and calculation result in February

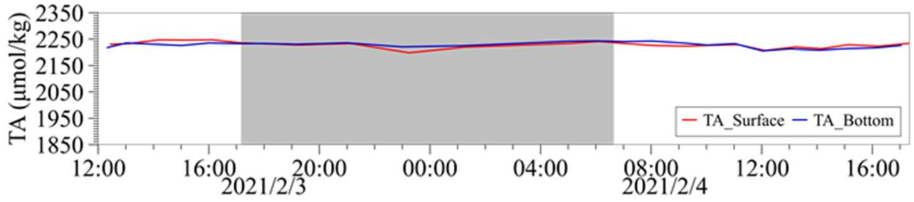

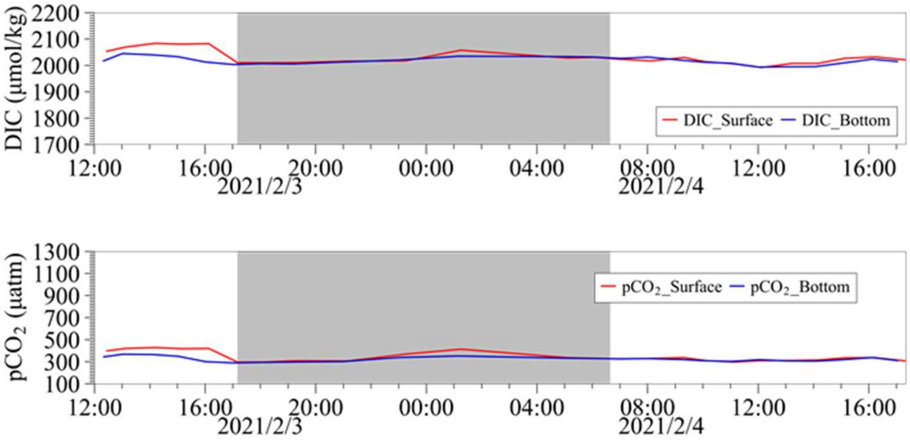

Figure 3.10 Experiment A_T , DIC results, and calculated pCO_{2sw} results for water samples collected in February

Although in this time's survey, phytoplankton concentration is higher and the light condition is better than December, even the effect of the photosynthesis on pH can be observed to some extent, we could not see the explicit influence on the other carbonate parameters. A_T(2195-2250$\mu mol/kg$), DIC (1990-2090$\mu mol/kg$) and pCO_{2sw} (290-430μatm) becomes higher when river water inflows, however, at 1 am of Feb.4th, surface A_T was higher when the salinity is lower, showing that A_T is not totally proportional to salinity. A conclusion can be drawn that during this time's survey, water exchange is a more dominant influence factor than biological activities.

3.4 Time series sampling in 2021 April

3.4.1 Survey result in April

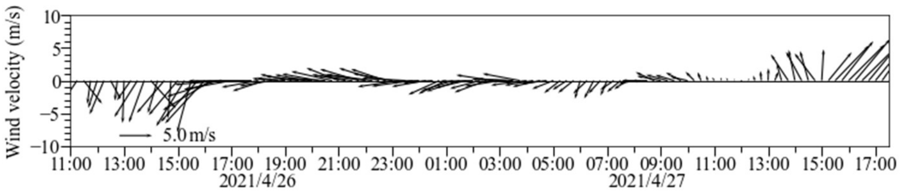

Figure 3.11 Wind measured at monitoring station during the survey in April

Different from the former two surveys, the survey in April was conducted during spring tide, so the tide level change is larger as shown in Figure 3.12.

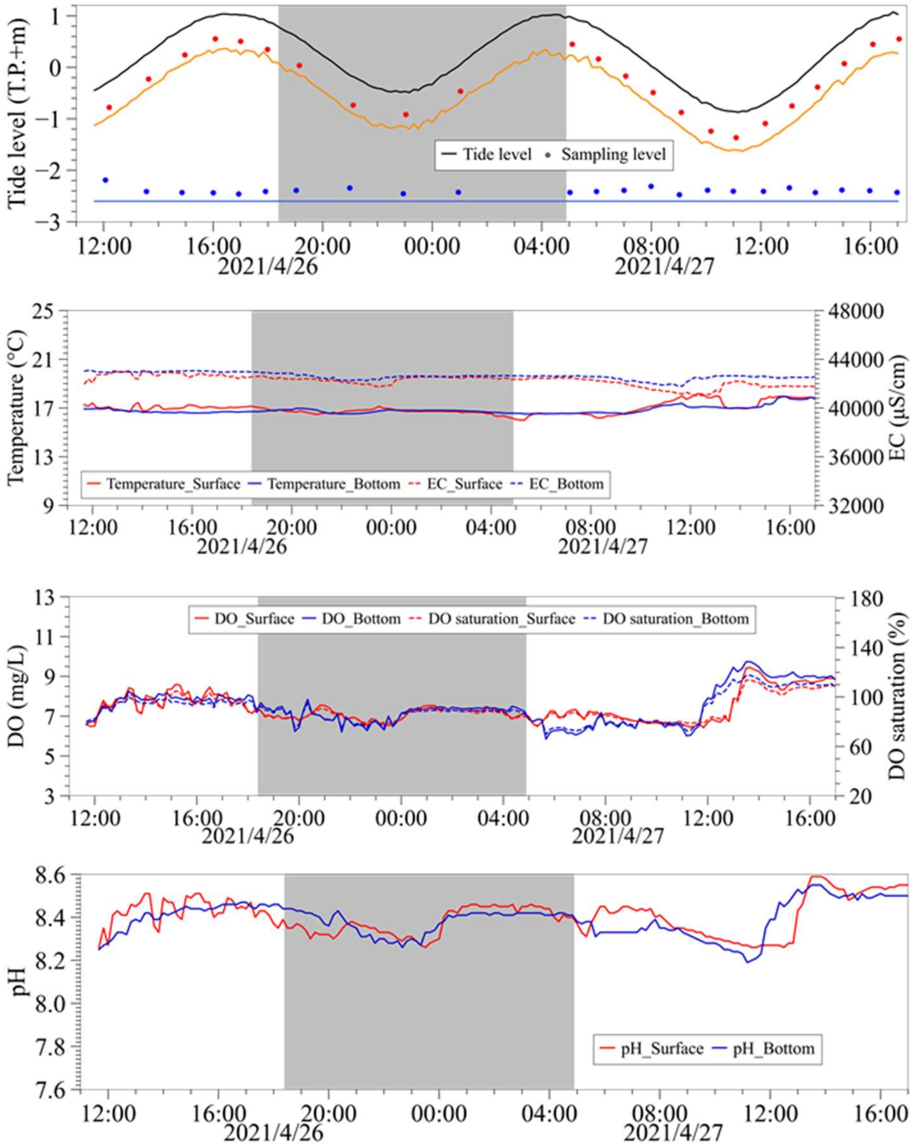

Figure 3.12 Tide level, Temperature, EC, DO, pH data captured by mooring system in April

The temperature difference between surface and bottom in April is close, but the overall temperature is much higher than the former two months that the scale for AAQ temperature data is different. In April.26th afternoon and April.27th afternoon, especially 27th, the temperature gradient can be observed along with the water depth. The strong sunlight is thought to be the heat source, in contrast, the lower surface temperature can be observed at the midnight due to heat dissipation. Salinity in this time's survey is a bit lower than before, and since it was spring tide, salinity change caused by river water inflow is also larger than before, on the 27th afternoon both the AAQ salinity graph and the mooring system graph have a significant drop.

Rising temperature cause the oxygen saturation in the seawater to lower than before, however a notable spike in both DO and pH can be observed on the 27th afternoon, this time the effect of photosynthesis was very clear that it was the oxygen generated by photosynthesis and the carbonic acid consumed led to this phenomenon. The higher phytoplankton concentration and good light condition in Figure 3.13 (d) and (e) agreed with this explanation. Additionally, the DO and *chlorophyll-a* data captured by AAQ illustrated that the photosynthesis on the 27th afternoon was much stronger than the 26th afternoon.

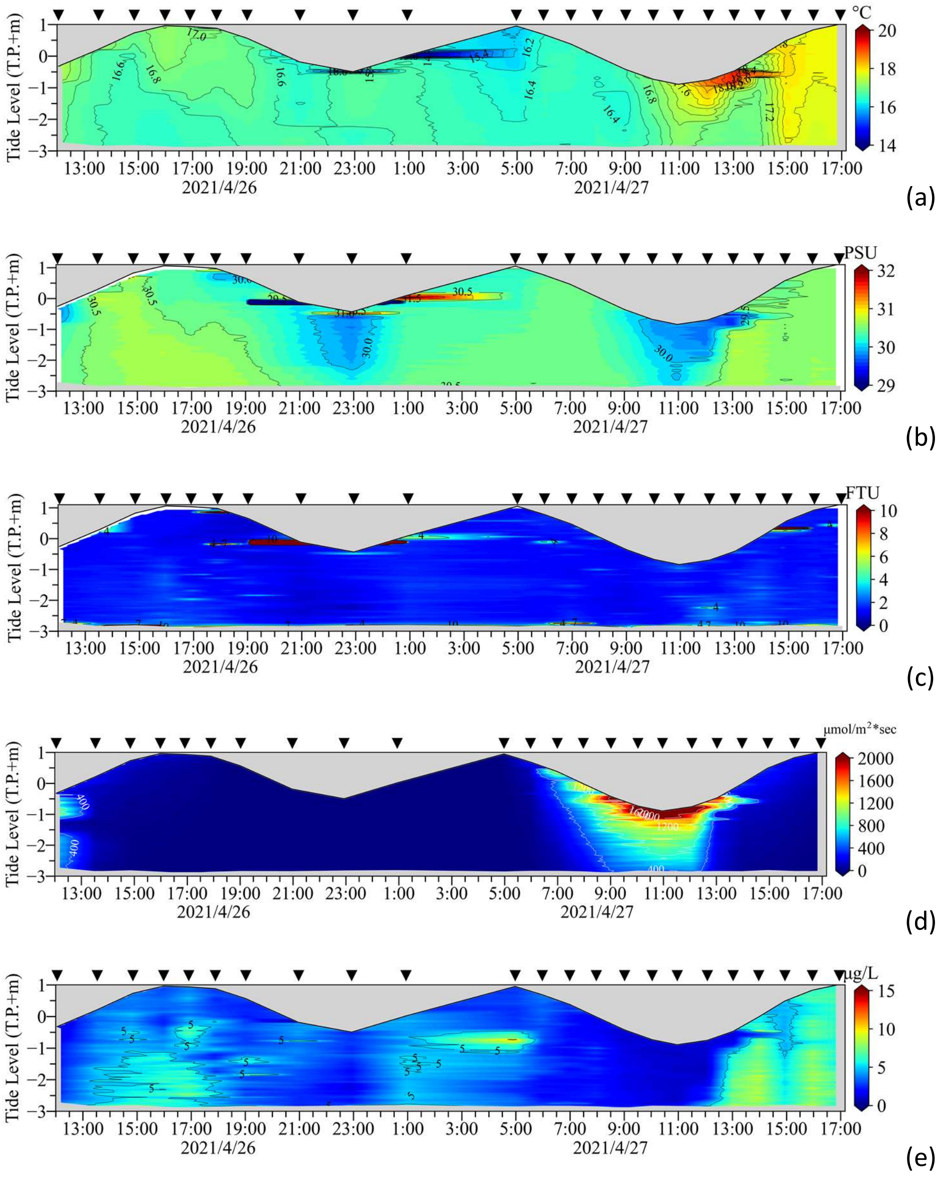

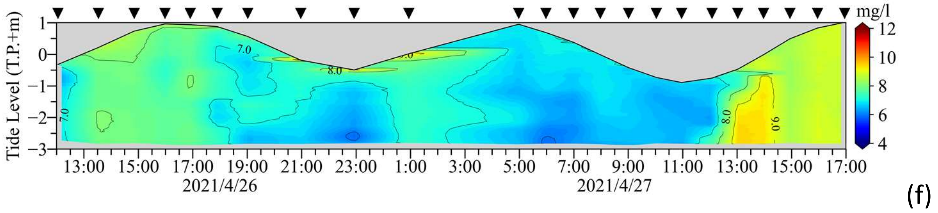

Figure 3.13 AAQ Water parameter data in April. (a)Temperature, (b)Salinity, (c)Turbidity, (d)Light quantum, (e)*Chlorophyll-a* concentration, (f)DO

3.4.2 Experiment and calculation result in April

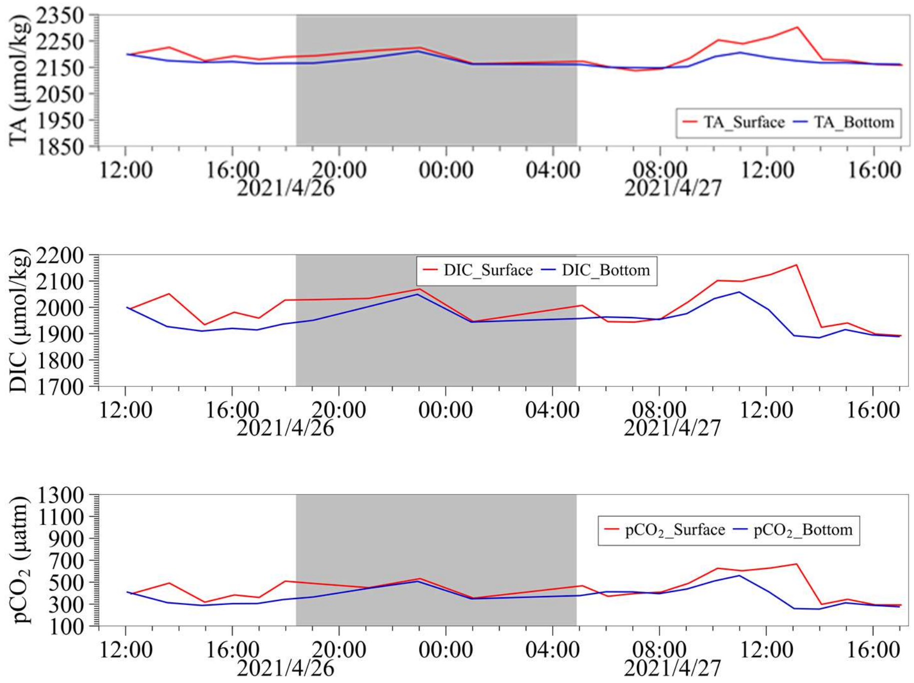

Figure 3.14 Experiment A_T , DIC results, and calculated pCO_{2sw} results for water samples collected in April

Photosynthesis consumed the DIC in the water, and DIC was very easily influenced that it was much lower than former surveys (1880-2160 $\mu mol/kg$), but it became larger when river water inflowed. pCO_{2sw} measures the amount of carbon dioxide dissolved in water, so it had a similar changing trend as DIC (254-665 μatm). Salinity in this time's survey is lower than before, which may explain the comparatively lower A_T(2150-2310 $\mu mol/kg$). Some study implies that A_T of seawater is changed during photosynthesis, because of the alkalinity of the organic constituents of marine phytoplankton and the uptake of NO_3^- and NH_4^+ [35, 36]. While main total alkalinity contributor $[HCO_3^-]$ and $[CO_3^{2-}]$, defined as carbonate alkalinity (A_C) is consumed during photosynthesis, which may lead to lower A_T. This further relates to the chemical equilibrium of the carbonate system that it would be hard to judge how the photosynthesis influenced the A_T only from this time's data. At 13:00 of April 27th, bottom pCO_{2sw} and DIC reached the lowest value in this time's survey, at the same moment, surface DIC and pCO_{2sw} was the highest for the river water influence. We can say that at this moment, in the bottom layer phytoplankton activity influence suppressed water exchange influence, while in the surface layer, water exchange influence is still more dominant to the carbonate system.

3.5 Time series sampling in 2021 June

3.5.1 Survey result in June

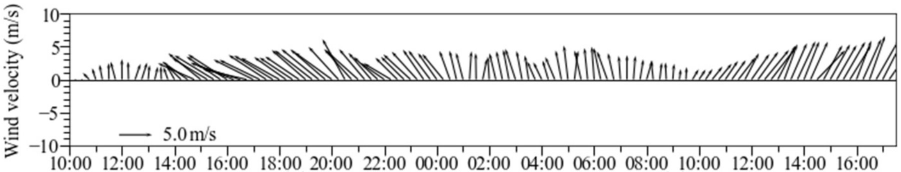

Figure 3.15 Wind measured at monitoring station during the survey in June

In the survey of June, the wind continuously below ranging from east-south to west-south direction. The tide on June 1st was mid-tide, and on June 2nd it was the neap tide.

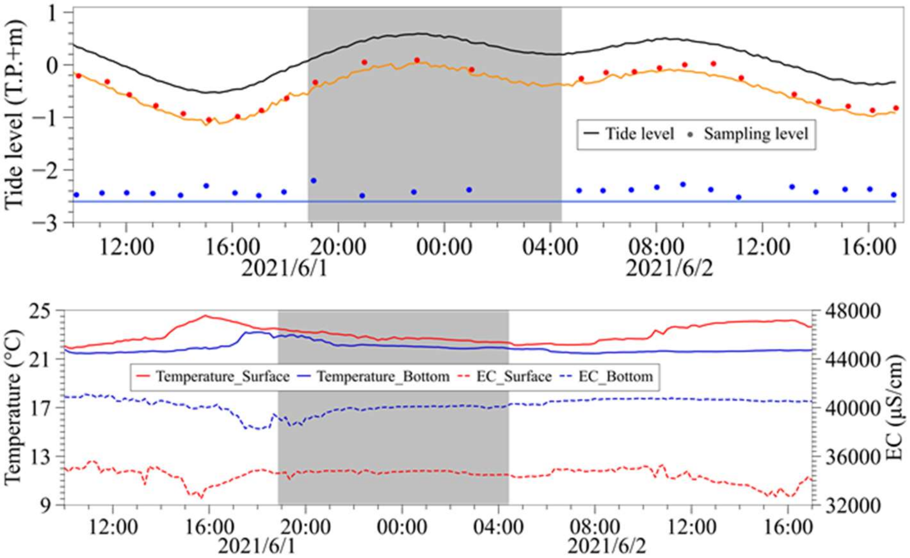

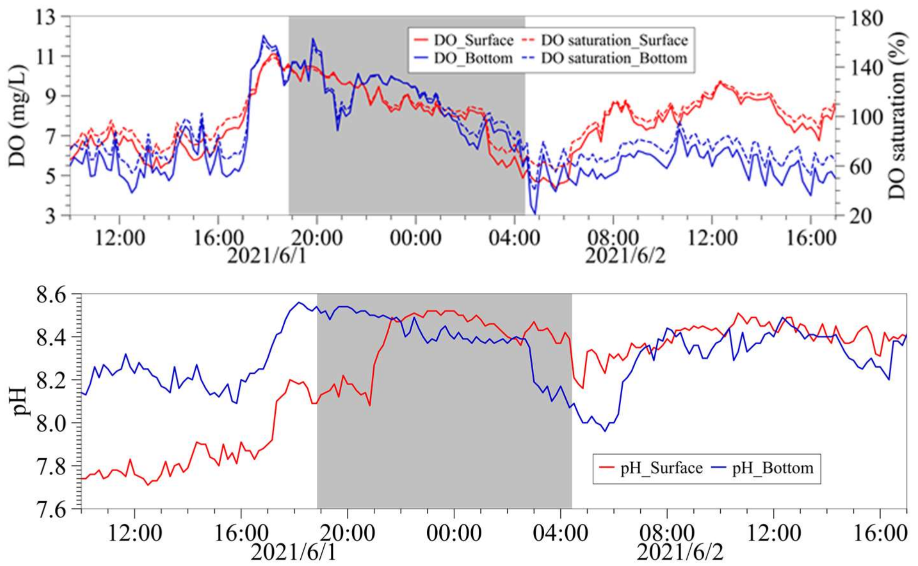

Figure 3.16 Tide level, Temperature, EC, DO, pH data captured by mooring system in June

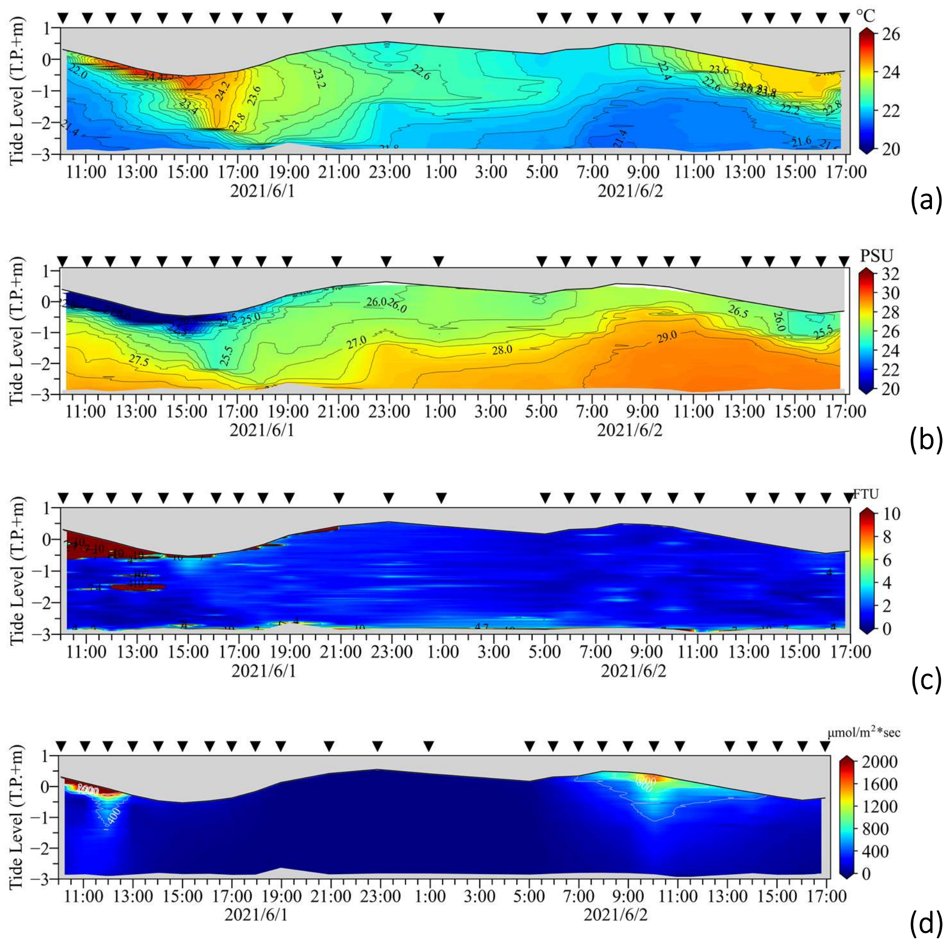

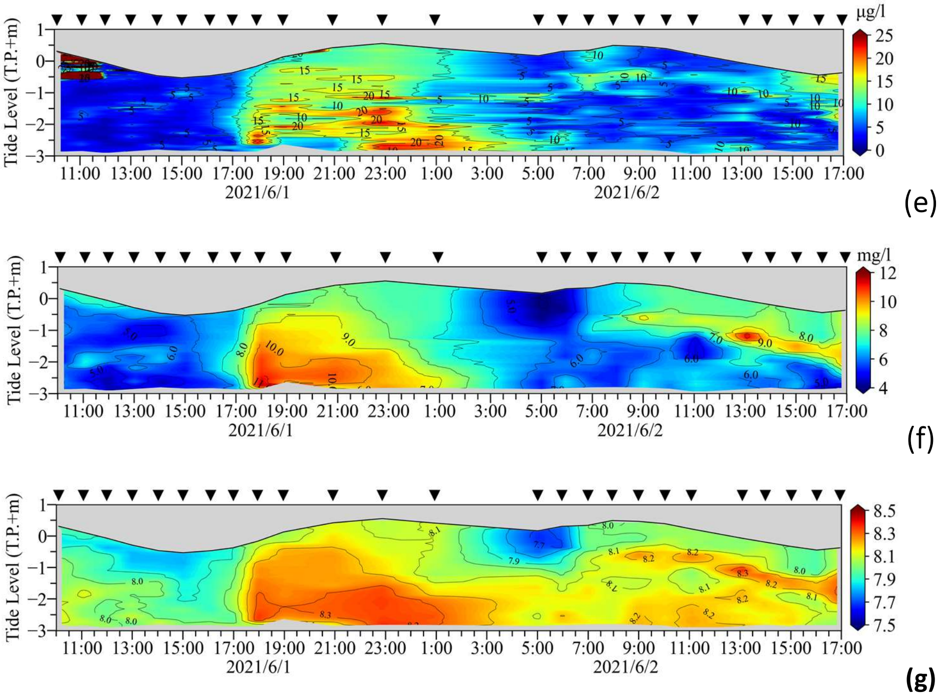

Figure 3.17 AAQ Water parameter data in June. (a)Temperature, (b)Salinity, (c)Turbidity, (d)Light quantum, (e)*Chlorophyll-a* concentration, (f)DO, (g)pH

Water temperature in June was the highest in these four times of surveys with a distinct gradient from surface to bottom particularly in the afternoon, partly because of the high temperature in the field, and partly because of the sunlight. The EC plotting of the surface and bottom layer in Figure 3.16 was totally separated, and salinity plotting in Figure 3.17(b) shows the range from 29 ppt in the bottom to lower than 20 ppt in the surface. The rainfall at the midnight of June.1st is thought to be the reason to cause the low salinity in the surface, and this rainwater is also collected by the river that even in the low tide period in June.2nd, lower salinity than 26 ppt can be observed in the surface layer.

Turbidity and *chlorophyll-a* concentration was unusually high in the surface layer of June.1st, garbage and seagrass were observed in the surface water, which is brought to the sampling sight by the south wind when the wind direction changed from south to east-south, this phenomenon disappeared.

The weather of June 1st was sunny, and a high *chlorophyll-a* concentration was observed at the Urayasu monitoring station. In Figure 3.17(e)(f)(g), the high DO, pH, *chlorophyll-a* water captured by AAQ starting from 17:00, is thought to be brought to the sampling site by the east-south wind. A similar spike in pH and DO can be seen in Figure 3.16, in addition, because of the rainwater influence, surface pH was much lower than the bottom layer. During the night, because of the respiration of phytoplankton, DO was gradually consumed and pH gradually dropped for the CO2 generated in respiration. On June.2nd afternoon, high *chlorophyll-a* concentration was only observed on the surface, thus photosynthesis only caused DO and pH to rise in the surface, but surface pH was again influenced by river water inflow to be lower.

3.5.2 Experiment and calculation result in June

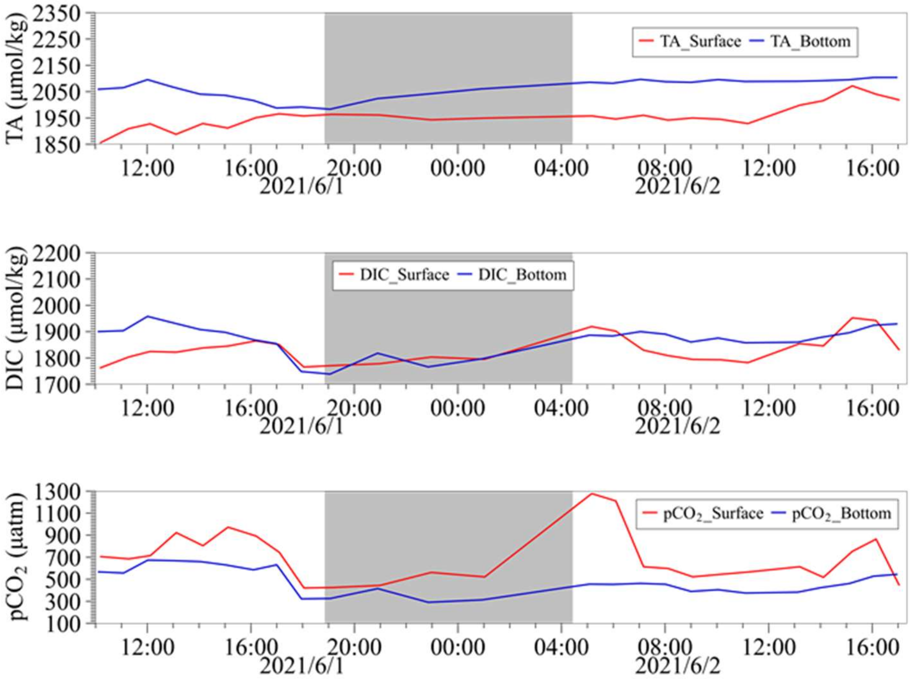

Figure 3.18 Experiment A_T, DIC results, and calculated pCO_{2sw} results for water samples collected in June

Variance in A_T and pCO_{2sw} was the largest among the surveys. Just as the plotting of EC in Figure 3.16, on account of the influence from salinity to A_T, surface and bottom A_T the difference was very large. The distance between the plotting line was larger when the salinity gradient along the depth is large, vice versa. Surface water containing high phytoplankton concentration in June.1st morning consumed DIC in the surface, so the surface DIC is apparently lower than the bottom. After the wind direction changed, DIC concentration in surface and bottom became similar, and at around 17:00 photosynthesis consumed DIC again that both bottom and surface DIC dropped. In the nighttime, respiration caused the DIC in the water to gradually rose. On June.2nd, photosynthesis in the surface layer led to low DIC in the surface, but river inflow at around 15:00 made surface DIC higher again.

pCO_{2sw} change is similar to DIC, but different from the survey in April, though surface DIC was sometimes lower than the bottom, surface pCO_{2sw} is always higher than the bottom, which might be because of the uptake of atmospheric CO2 in the surface layer when CO2 concentration is low. It was remarkable that at the dawn of June.2nd, pCO_{2sw} reached peak of all these four times of survey, indicating that the day-night change of $\mathrm{pCO}_{2\mathrm{sw}}$ will be very large when biological activities thrived in the water environment.

3.6 Permutation Feature Importance for Regression

Feature importance is the scores assigned to input features to a predictive model, illustrating the relative importance of each feature when making a prediction, and permutation feature importance is a technique for calculating relative importance scores that is independent of the model used. In this section, feature importance scores are calculated for regression of total alkalinity and $\mathrm{pCO}_{2\mathrm{sw}}$ using the Random Forest model, which is reported to be able to make an unbiased measurement [37]. Here, the purpose of feature selection is to provide an insight into the field data, highlighting which features may be most relevant to the target.

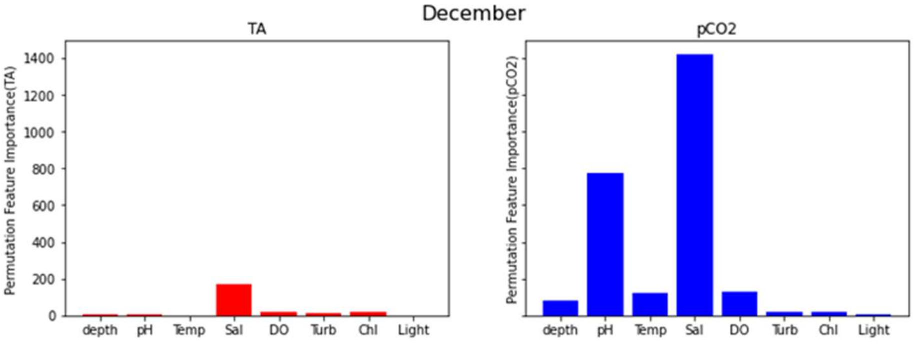

(a)

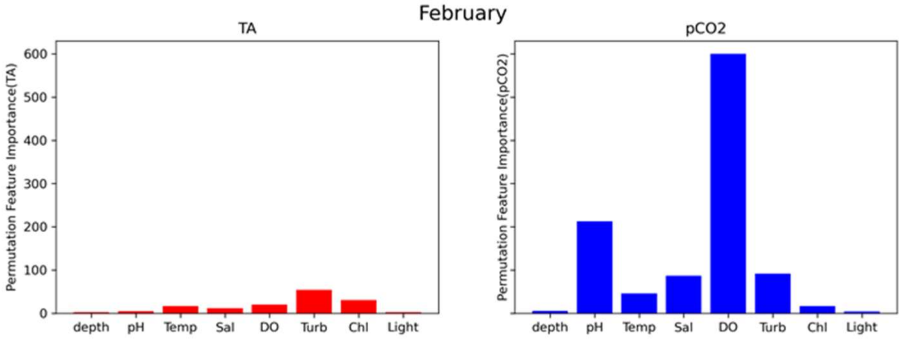

(b)

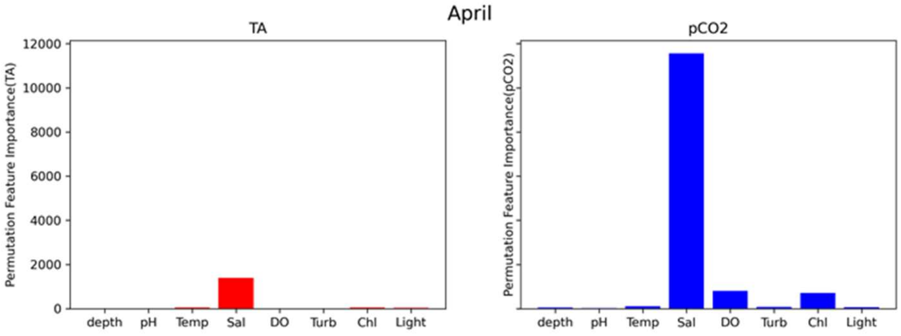

(c)

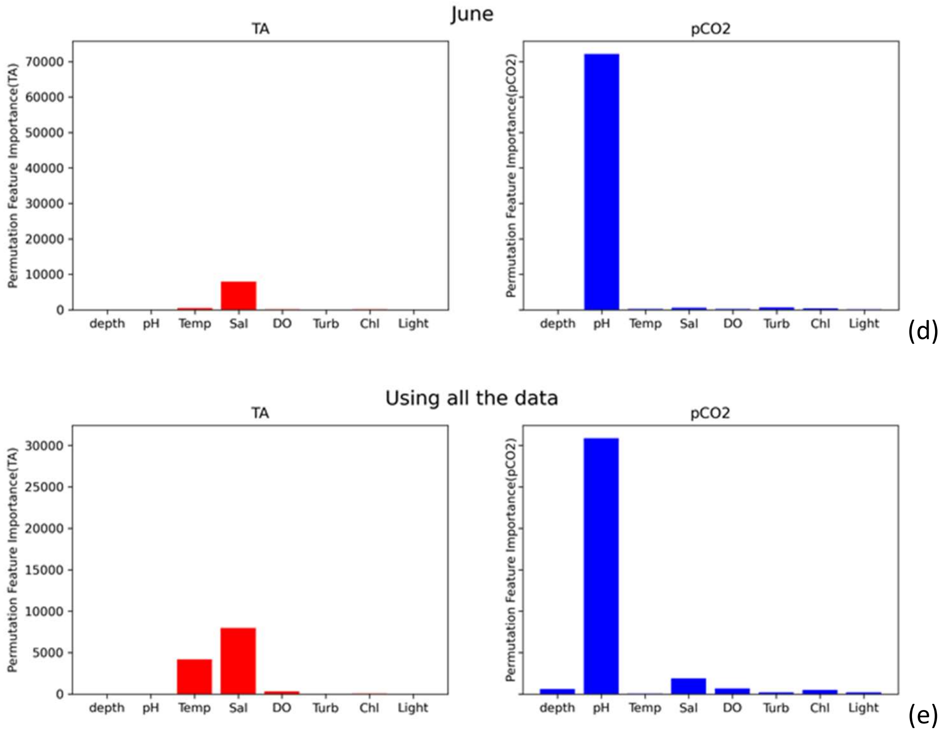

Figure 3.19 Permutation Feature Importance result. (a) Field data in December; (b) Field data in February; (c) Field data in April; (d) Field data in June; (e) All the data collected in the field.

Comparing the feature selection result for Total alkalinity from Figure 3.19(a) to (e), salinity was the most influential factor in December, April, and June. In December and February, the score for salinity is lower, the reason might be comparatively steady salinity in the field. In February, turbidity was even more important than salinity, this might be because the strong southwest wind which disturbed the water brought seawater with higher total alkalinity to the sampling site. In Figure 3.19 (e), the temperature is the second influential factor. Theoretically, total alkalinity itself is a conservative measurement, so it is not much influenced by temperature, but the specific gravity that is commonly used to converse to salinity can be influence by temperature. Besides, the sea surface temperature is mentioned to be often inversely proportional to A_T [38]. So that instead of developing a regression equation between salinity and A_T season by season [14], the temperature can be added to reflect the seasonal change.

About the feature selection result for$\mathrm{pCO_{2sw}}$, in Figure 3.19 (e), pH is the most important factor, but in Figure3.19 (a), (b), and (c), it is not. pH as one term of the seawater carbonate system and input to calculate $\mathrm{pCO_{2sw}}$, it is supposed to be highly related to $\mathrm{pCO_{2sw}}$. In the survey of June, because of the rainfall the midnight before, the pH range in the water was very large, from 7.6 to 8.5. In this case, the influence of pH was overwhelmingly stronger than other parameters, while in the survey of other months, the pH range was rather smaller. In the survey of December and April, salinity becomes the most vital factor, and river water inflow can be considered as the reason.

River water has lower salinity and higher CO2 concentration than the sampling site, so the $\mathrm{pCO_{2sw}}$ can somehow be related to salinity. Springtide in the survey of April and the north wind in the survey of December induced more river water inflow, therefore the importance of salinity became larger. In Figure 3.19(b), DO is most significant, and in Figure 3.19(c), DO is secondly important followed by *chlorophyll-a* concentration. Some studies pointed out the negative correlation between DO and $\mathrm{pCO_{2sw}}$ [11, 39], and biological reactions including photosynthesis and organic matter decomposition are thought to be the reason. In April, the similar importance of DO and *chlorophyll-a* concentration indicated the high contribution of photosynthesis.

3.7 Regression for Total alkalinity and $\mathbf{pCO_{2sw}}$

3.7.1 Univariate regressions

The most influential factor picked out in section 3.6 was used for univariate regression for total alkalinity and $\mathrm{pCO_{2sw}}$.

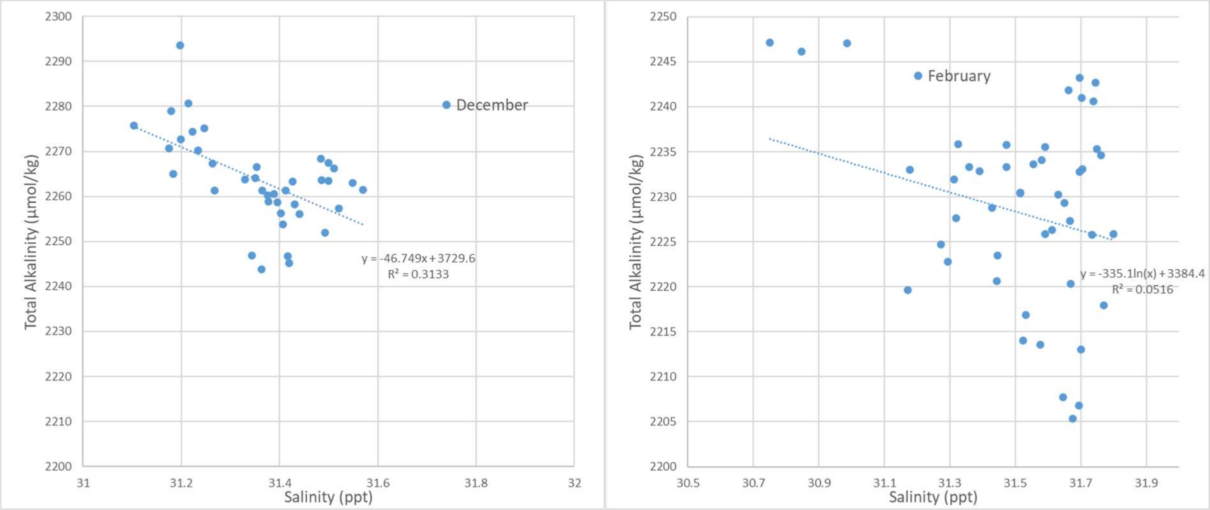

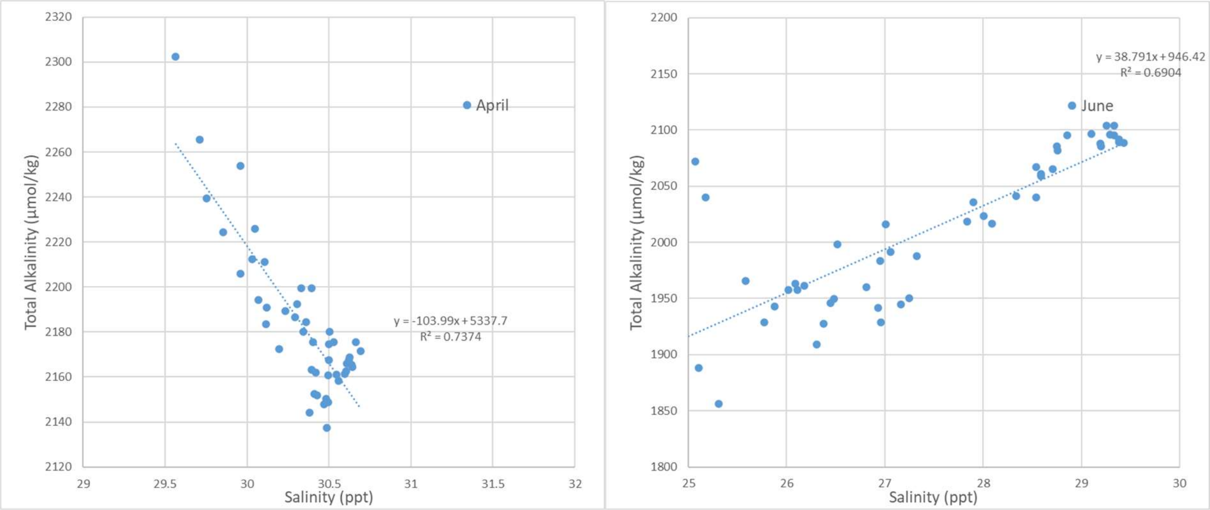

Figure 3.20 Total Alkalinity-Salinity relation for each time's survey

Unlike the salinity-A_T regression line developed for Tokyo Bay with positive correlation and a high coefficient of determination value[12], our survey results in December and April shows a negative correlation between A_T and salinity. The river water contains lower salinity and higher A_T then the sampling site, which is thought to be the explanation of negative correlation. In June, rainfall caused a large salinity gradient along with the water depth, thus only in this time, positive correlation between salinity and A_T was observed. While in February, the seawater was disturbed by the south wind, water in the bay was moved to the sampling location and the relation between salinity and A_T cannot be seen.

What's more, we can see from the x-y scale difference that when the salinity range is large, it is a practical approach to regress the A_T from salinity, but in smaller salinity scale, using only the salinity is not able to explain the variation in A_T.

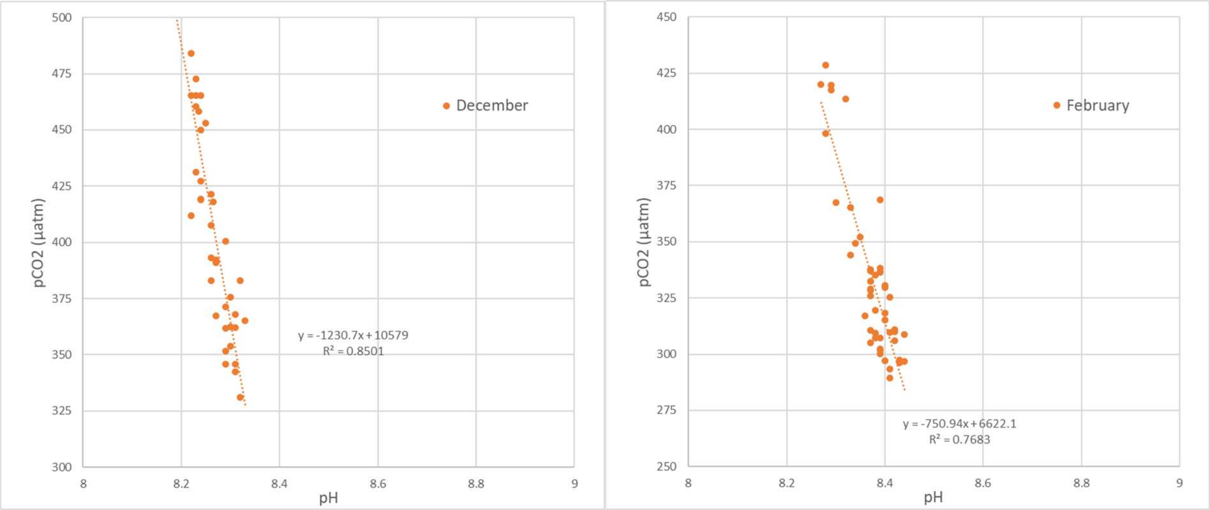

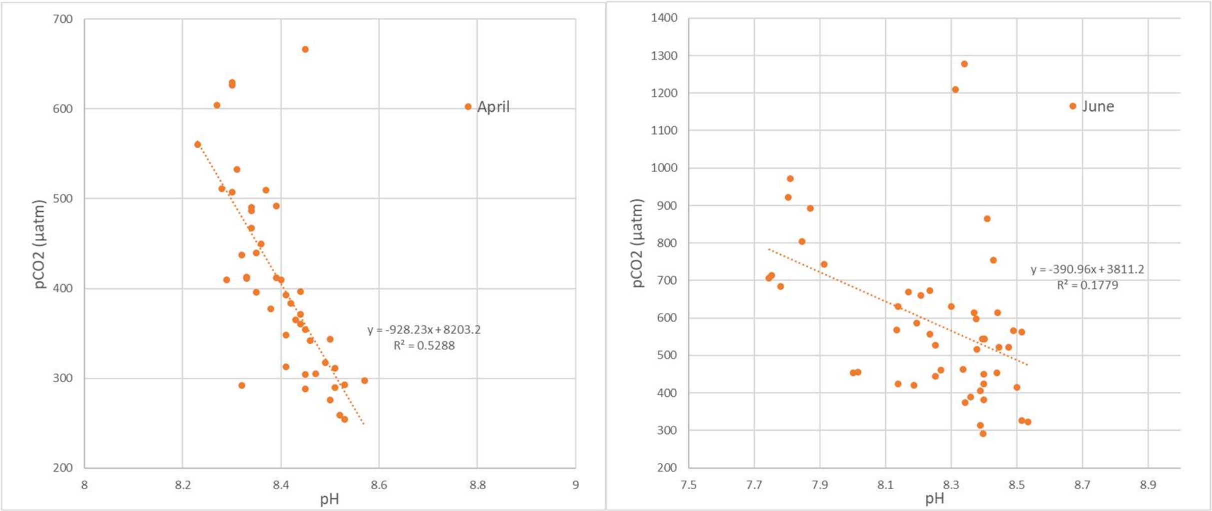

Figure 3.21 $\mathbf{pCO_{2sw}}$-pH relation for each time's survey

The negative correlation between pH and $\mathrm{pCO_{2sw}}$ matches with the former research that the relation between them is more like a logarithmic curve [11]. When the pH range is lower, the slope of the pH-$\mathrm{pCO_{2sw}}$ the line will be steeper. Though in the plotting of the survey in June, the data points scattered dispersedly, and the coefficient of determination value was low, pH is still evaluated as the most influential factor in Figure 3.19 (d), showing that simple linear and no-linear model is not enough to describe the ph-$\mathrm{pCO_{2sw}}$ relation in this case.

3.7.2 Cause of underestimation of $\mathbf{pCO_{2sw}}$

Figure 3.22 compares the total alkalinity ($\mathrm{A_T}$) estimated from salinity and the experiment $\mathrm{A_T}$ results with our data, in December, February, and April, the $\mathrm{A_T}$ in the field is completely underestimated and many data points fall out of the standard deviation range of the regression line, which is 34 [12].

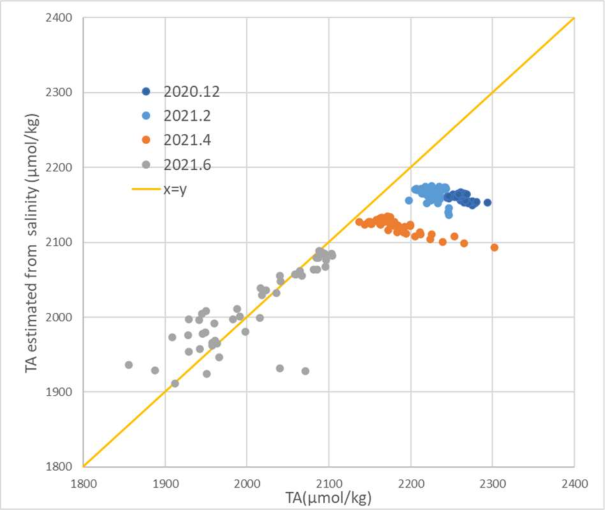

Figure 3.22 Comparison between the Total Alkalinity estimated from salinity and the experiment result.

The left side graph of Figure 3.23 shows that most of the data points are severely underestimated that it is hard to say this $\mathrm{pCO_{2sw}}$ result is meaningful. Therefore, it is necessary to reconsider the $\mathrm{A_T}$ and $\mathrm{pCO_{2sw}}$ estimation method.

To figure out how much underestimation of $\mathrm{A_T}$ can influence on $\mathrm{pCO_{2sw}}$ result, experiment $\mathrm{A_T}$ and field pH were used to calculate $\mathrm{pCO_{2sw}}$ as a comparison in the right side of Figure 3.23. Comparing to the left side, these two plotting is almost identical, therefore the subtraction of these two estimation results is further performed and plotted in Figure 3.24. Results show that the difference caused by $\mathrm{A_T}$ estimation is less than 35 $\mu\mathrm{atm}$, so a guess can be made that pH is the main contributor to this inconsistency in $\mathrm{pCO_{2sw}}$.

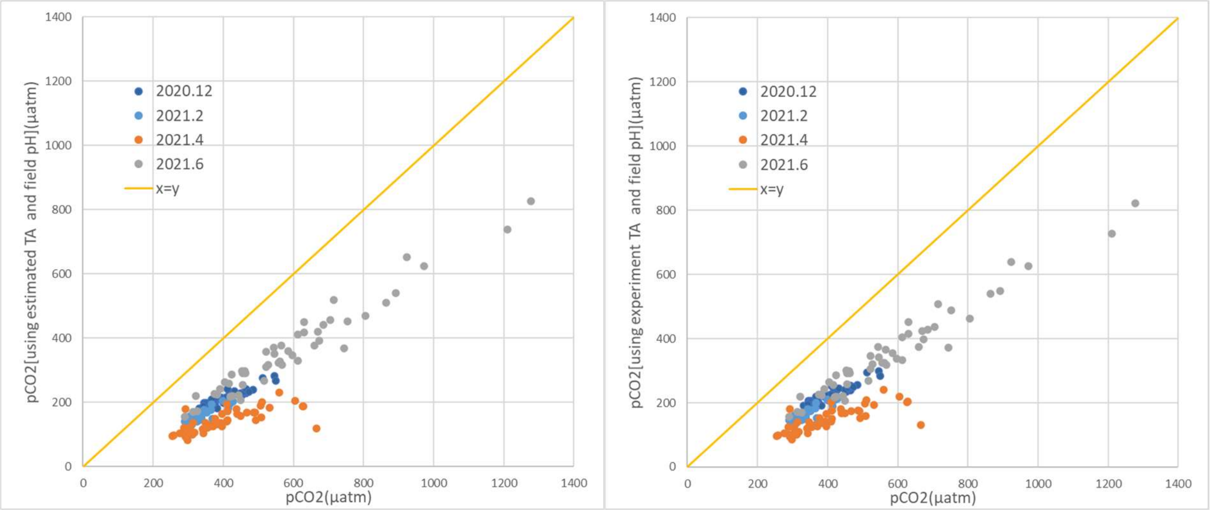

Figure 3.23 Estimation of the $\mathbf{pCO_{2sw}}$ in the field.

Left: $\mathbf{pCO_{2sw}}$ calculated using estimated $\mathbf{A_T}$ and field pH -- $\mathbf{pCO_{2sw}}$ calculated using experiment data;

Right: $\mathbf{pCO_{2sw}}$ calculated using experiment $\mathbf{A_T}$ and field pH -- $\mathbf{pCO_{2sw}}$ calculated using experimental data.

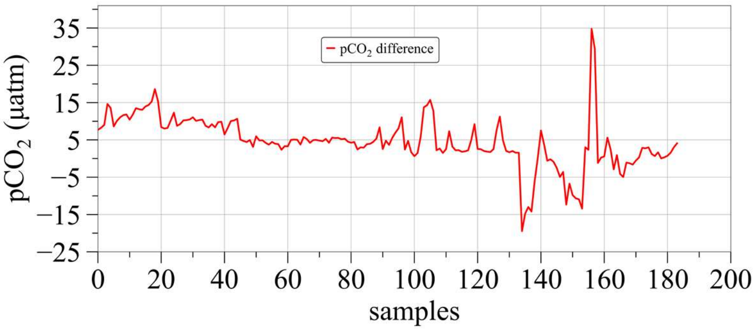

Figure 3.24 Difference in $\mathbf{pCO_{2sw}}$ estimation result.

$\mathbf{pCO_{2sw}}$ calculated with experiment $\mathbf{A_T}$ and field pH minus $\mathbf{pCO_{2sw}}$ calculated with estimated $\mathbf{A_T}$ and field pH.

A sensitivity test was performed using PyCO2SYS with the lab condition that temperature equals 20℃ and pressure equals 0 dbars, salinity is set to be 30 ppt, which is the average value for all the samples. For sensitivity test between A_T and pCO_{2sw}, pH is set to be the average value of 8.3. As shown in the left side of Figure 3.25, 50 $\mu mol/kg$ difference in A_T can only cause pCO_{2sw} difference of less than 10 μatm. For sensitivity test between pH and pCO_{2sw}, A_T is set to be the average value of 2165 $\mu mol/kg$, and the logarithmic relation can be observed that 0.1 difference in pH value at high pH range (8.5-8.6) caused around 30 μatm difference in pCO_{2sw}, while 0.1 difference in pH value at low pH range (7.7-7.8) caused pCO_{2sw} difference of more than 200 μatm. pH is a much more influential factor to pCO_{2sw} than A_T.

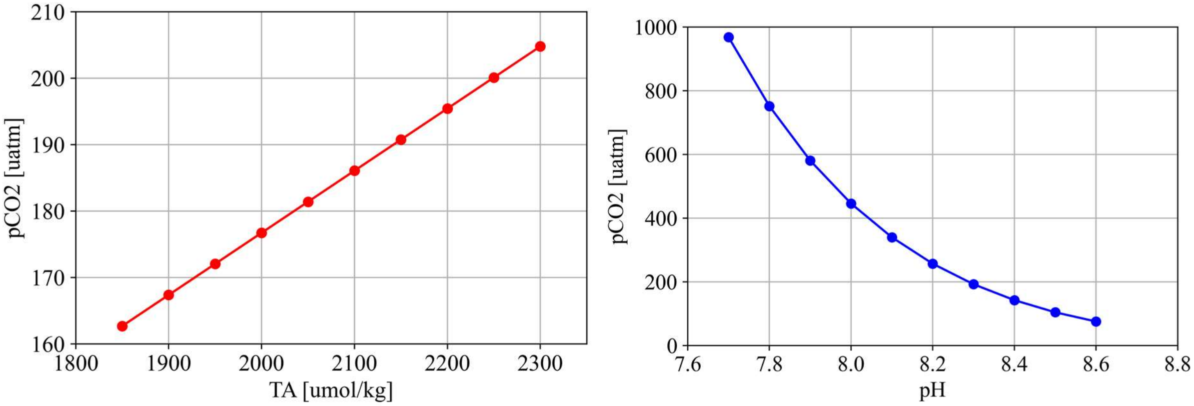

Figure 3.25 Sensitivity test.

Left: pCO_{2sw}—total alkalinity sensitivity; right: pCO_{2sw}—pH sensitivity.

In the experiments, it was found that sample pH measured under the lab condition is usually lower than the pH measured under the field condition. Also, CO2SYS itself is possible to calculate the field pH using data measured in experiments that temperature, as well as pressure difference between field and lab, is thought to be the cause.

Figure 3.26 shows the subtraction result between the measured field pH and the calculated field pH. The averagely larger than 0.1 difference is thought to be the reason for the underestimation of field pCO_{2sw}. Furthermore, $\Delta pH - pH$ plotting in Figure 3.27 illustrated that the ΔpH distributes in the comparatively sensitive range that the least pCO_{2sw} difference caused by ΔpH (from 8.2 to 8.3) will be 64.6 μatm.

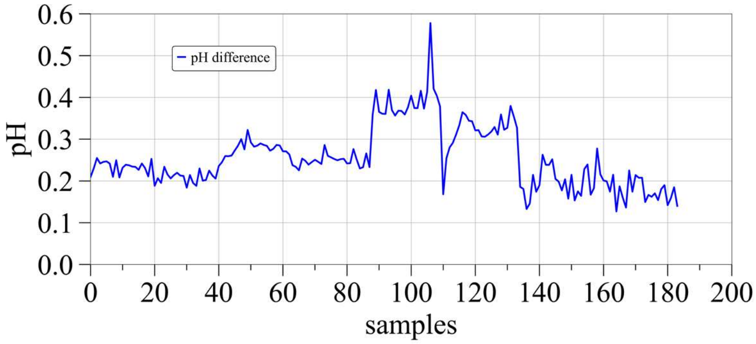

Figure 3.26 Inconsistency in field pH data.

pH measured in field minus pH in field condition calculated by PyCO2SYS.

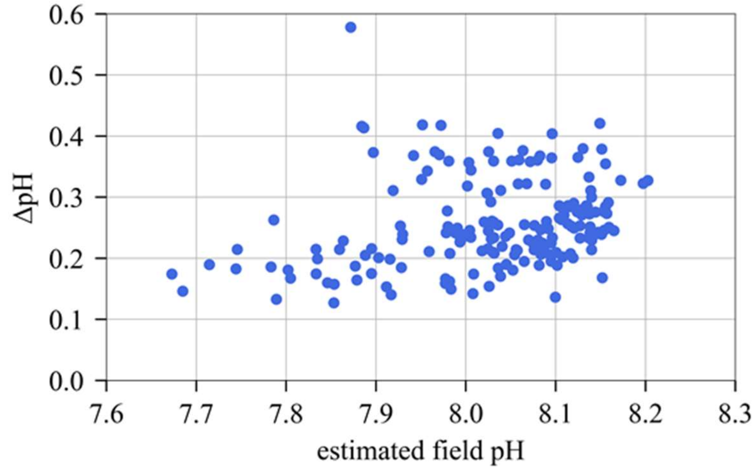

Figure 3.27 $\Delta\mathrm{pH}$ distribution on pH scale

3.7.3 Multivariate regression

Though the measured field pH data is biased from the theoretical field pH data, high relation between field pH and $\mathrm{pCO_{2sw}}$ can still be seen in section 3.7.1, which states that measured pH data is still meaningful. Unlike in the lab condition that we can measure the pH value precisely, in the field condition, it is hard to guarantee the pH data is unbiased. Hence, to avoid the underestimation caused by inputting pH data into CO2SYS, a data-driven approach is applied in this study to relate the measured field pH to accurately estimated $\mathrm{pCO_{2sw}}$. A model to predict the $\mathrm{A_T}$ as an improvement to the $\mathrm{A_T}$- salinity equation is proposed as well. Since the size of the dataset is quite small, and all the features are already based on prior knowledge, traditional machine learning methods are used with training and testing set split to 6:4.

Although in section 3.6, temperature and salinity have already be judged as the most important factor to regress total alkalinity, the environment parameter combinations are still tested for the best result. Also, it is noticed that splitting the training and test dataset differently can cause the score of the model to be different, so the performance of each model is evaluated three times with a shuffled dataset, then the average score is calculated as the evaluation result. The coefficient of determination of each model on the test set with different input combinations is summarized from Table 3.2 for $\mathrm{A_T}$ and Table 3.3 for $\mathrm{pCO_{2sw}}$. This dataset is a rather simple one, so all the applied machine learning methods got quite high scores. Among the models, Random Forest is chosen for Total Alkalinity regression, and Gradient Boosting is chosen for $\mathrm{pCO_{2sw}}$ regression.

According to Figure 3.19 (e), salinity, temperature, and DO are fed into models as inputs following the importance of the features. Adding DO into the models has already caused a decrease in $\mathrm{A_T}$, so salinity and temperature are used as input and the algorithm with the best performance is Random Forest. For regression of $\mathrm{pCO_{2sw}}$, adding input features of pH, salinity, *chlorophyll-a,* DO and temperature leads to the increase of

R^2 score, but turbidity and depth leads to decrease of R^2. So, the input features can be decided with Gradient boosting having the best performance.

Table 0.2 coefficient of determination (R^2) of models on Test dataset (for A_T)

input Algorithm	Salinity	Salinity & Temperature	Salinity, Temperature & DO	Salinity, Temperature, DO, turbidity, chl-a, pH
Decision Tree	0.884	0.952	0.954	0.936
Linear Regression	0.855	0.897	0.885	0.875
SVR	0.842	0.889	0.885	0.874
Random Forest	0.920	0.968	0.963	0.961
AdaBoost	0.909	0.959	0.950	0.940
Gradient Boosting	0.903	0.960	0.949	0.959
Bagging	0.922	0.963	0.962	0.951
Extra Tree Regressor	0.891	0.941	0.910	0.933
Average of models	0.891	0.941	0.932	0.929

Table 0.3 coefficient of determination (R^2) of models on Test dataset (for pCO_{2sw})

input Algorithm	pH	pH & Salinity	pH, Salinity & Chl-a	pH, Salinity, Chl-a & DO	pH, Salinity, Chl-a, DO & Tur
Decision Tree	0.694	0.749	0.693	0.709	0.766
Linear Regression	0.678	0.720	0.787	0.799	0.748
SVR	0.069	0.521	0.634	0.661	0.656
Random Forest	0.723	0.809	0.812	0.916	0.864
AdaBoost	0.733	0.804	0.785	0.908	0.800
Gradient Boosting	0.727	0.790	0.809	0.909	0.867
Bagging	0.727	0.785	0.822	0.908	0.845
Extra Tree Regressor	0.666	0.823	0.836	0.622	0.608
Average of models	0.627	0.750	0.772	0.804	0.769

	pH, Salinity, Chl-a, DO & Temperature	pH, Salinity, Chl-a, DO, Temperature, & depth
Decision Tree	0.858	0.753
Linear Regression	0.841	0.869
SVR	0.803	0.786
Random Forest	0.907	0.896
AdaBoost	0.877	0.891

Gradient Boosting	0.921	0.887
Bagging	0.905	0.840
Extra Tree Regressor	0.876	0.524
Average of models	0.874	0.806

The R^2 results are much better than using only univariate regression in section 3.7.1, and the prediction performance of the trained models is tested in Figure 3.28. A similar graph to Figure 3.23 is plotted in Figure 3.29 to show the deviation of the predicted value from the true value.

Although most data lie on the “x = y” line in Figure 3.29, still some of the outliers can be seen on the graph. What is worth mentioning is that only 110 data are used to train the models, and it has already shown its desirable generalization ability. Marine chemistry is a mature discipline, and pH has already been proven to be a vital parameter in estimating the seawater carbonate system. This means if attempts are made to gather samples within the pivotal pH range, the reliability of the data-driven approach in this traditional discipline will be further enhanced.

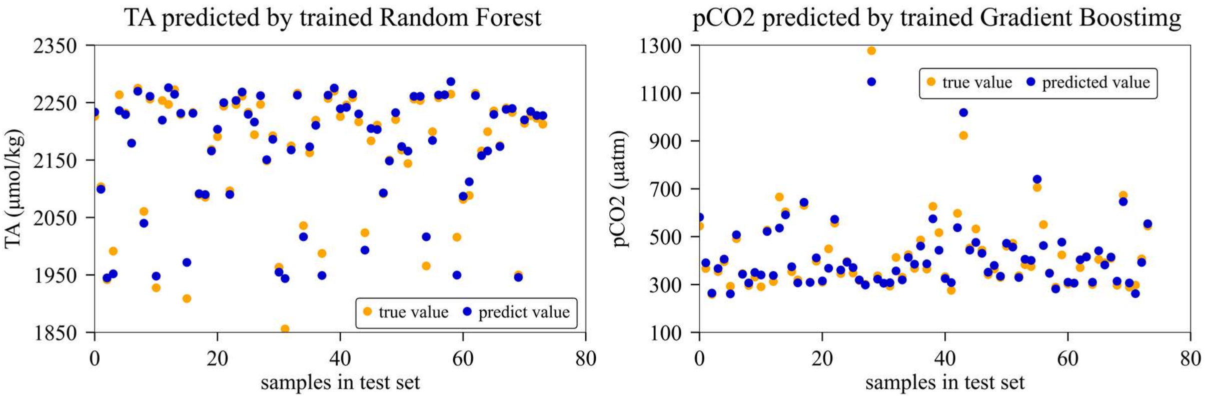

Figure 3.28 Comparison of predicted result and true result in the test set.

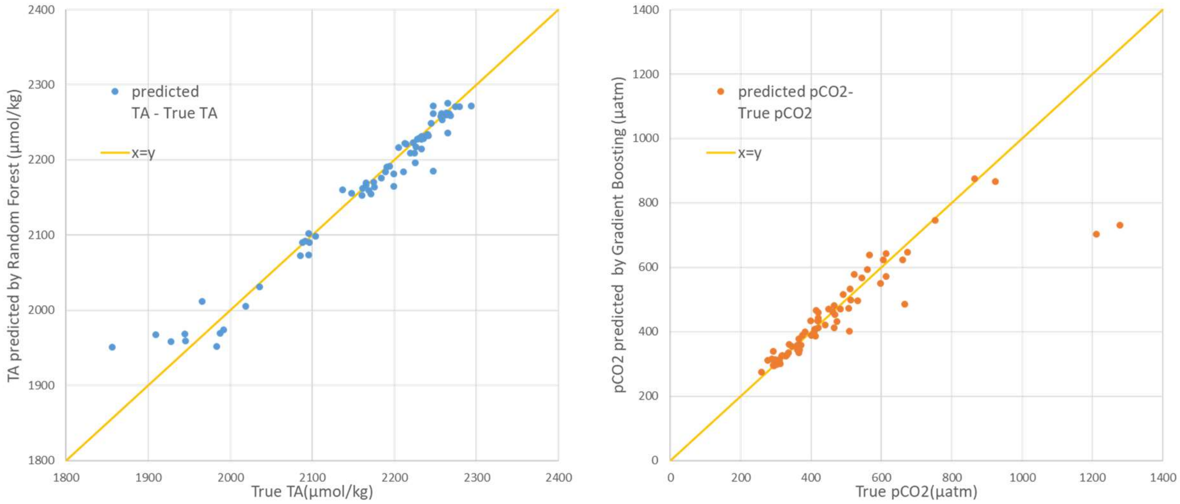

Figure 3.29 Estimation of A_T and pCO_{2sw} through machine learning.

left: A_T predicted using Random Forest model - A_T measured in experiments.

Right: pCO_{2sw} predicted by Gradient Boosting – pCO_{2sw} calculated from experimental data.

3.8 Time series A_T and pCO_{2sw} trend at Urayasu monitoring station

3.8.1 Time series A_T

The selected algorithms in section 3.7 were trained with all the data collected in the field, then used for prediction for total alkalinity and pCO_{2sw} using Urayasu monitoring data. Table 3.4 lists the total alkalinity range for all four times of surveys. Though our collected A_T data falls in the range between 2100 to 2300 $\mu mol/kg$, the prediction ability of the model is not limited within this range that predicted value as low as 1900 $\mu mol/kg$ can be observed on the figure.

Table 0.4 Total alkalinity range in our survey

December 24th -25th	2243.86-2293.6 $\mu mol/kg$
February 3rd – 4th	2198.16-2243.24 $\mu mol/kg$
April 26th – 27th	2137.27-2302.33$\mu mol/kg$
June 1st – 2nd	2137.27-2302.33 $\mu mol/kg$

In June, a sudden drop in A_T predicted by linear function can be seen on the graph, this coincided with the sudden salinity drop from 25 ppt to 15 ppt of the monitoring data. This unusual low salinity and its sudden recovery is thought to be caused by sensor maintenance, however, the result predicted by the Random Forest model developed in this study remains in the reasonable range. Comparing the orange line representing Random Forest model result and the red line representing the linear model result. On a broad scale, they have a similar trend, but on small scale, they have opposite fluctuation, which might be caused by the river water inflow at the sampling site. River water with lower salinity and higher $\mathrm{A_T}$ lead to a negative correlation between salinity and $\mathrm{A_T}$, but whether the water at the Urayasu monitoring station accepted enough river water influence to follow this trend still needs to be identified. Yet at least it has been approved that the linear correlation is not robust enough to describe the phenomenon at the river mouth.

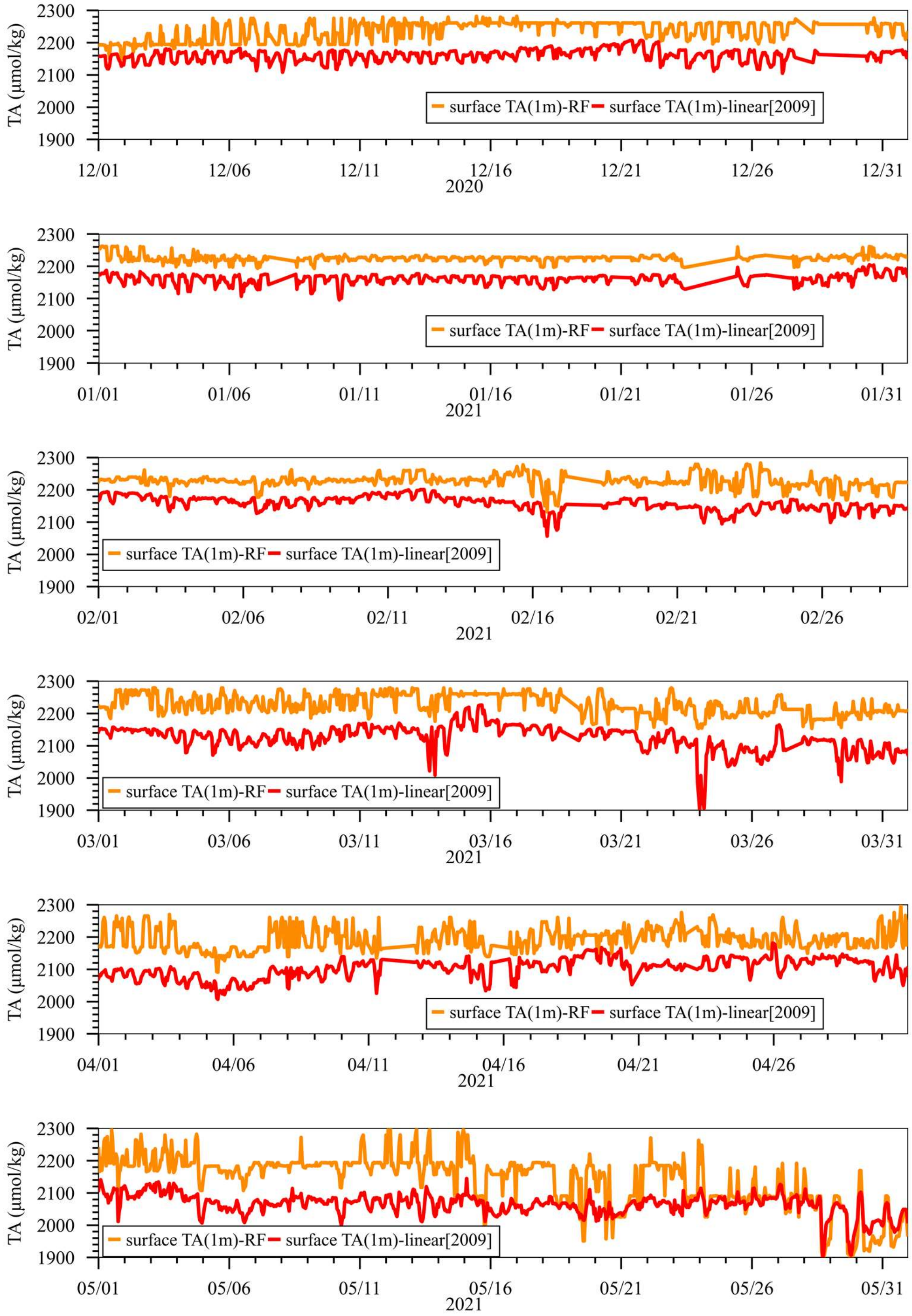

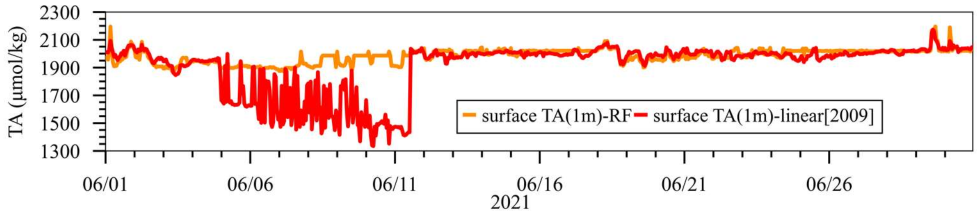

Figure 3.30 surface Total alkalinity prediction result at Urayasu station Using Random Forest model developed in this study, and the prediction results of $\mathrm{A_T}$-salinity equation[12]

The sampling depth of the surveys in this study ranges from 0.5 m to more than2.5 m, so the $\mathrm{A_T}$ is also predicted in the middle layer as a contrast. The results plotted in Figure 3.31 shows that the surface $\mathrm{A_T}$ and the middle layer $\mathrm{A_T}$ is rather close. In May and June, the salinity difference in surface and middle layers became larger that the $\mathrm{A_T}$ difference also became larger. Similarly, on around March 24th and March 14th, lower surface $\mathrm{A_T}$ is caused by lower surface salinity as well. Though the temperature is inputted as a feature, the shot-term influence of temperature on $\mathrm{A_T}$ is very minor that it basically cannot be observed. Temperature is more likely to reflect $\mathrm{A_T}$-salinity relation changes season to season.

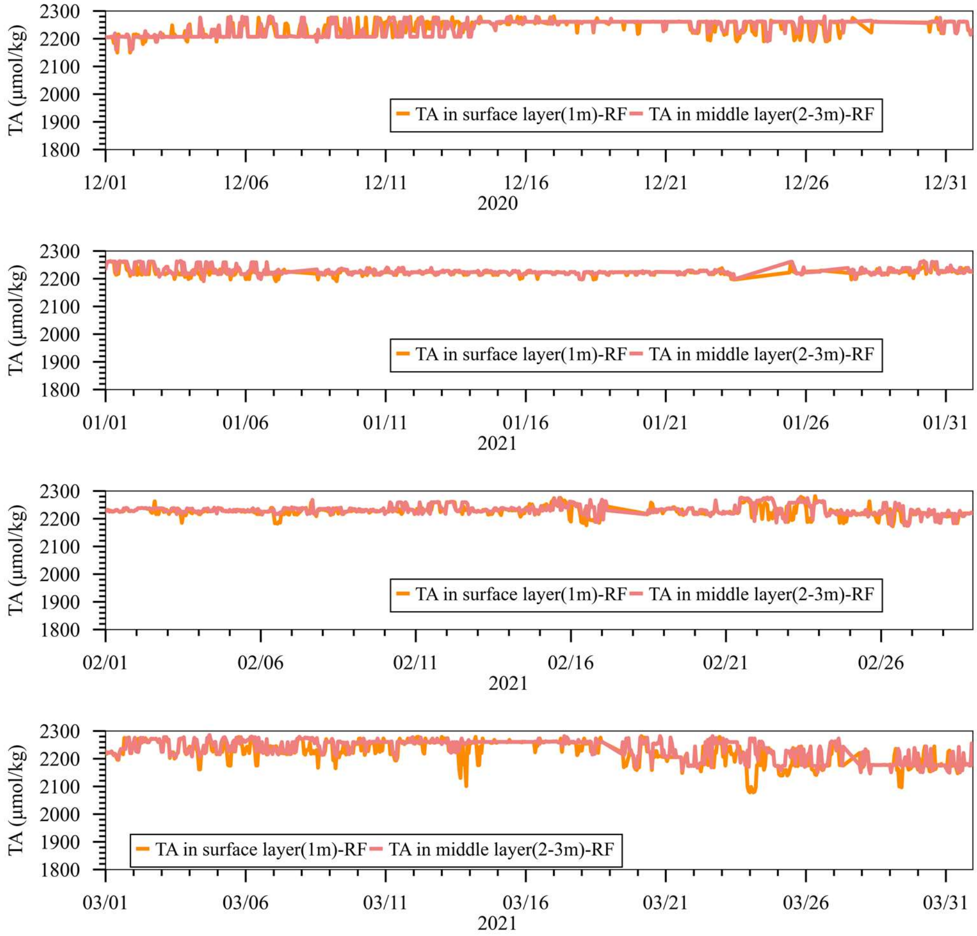

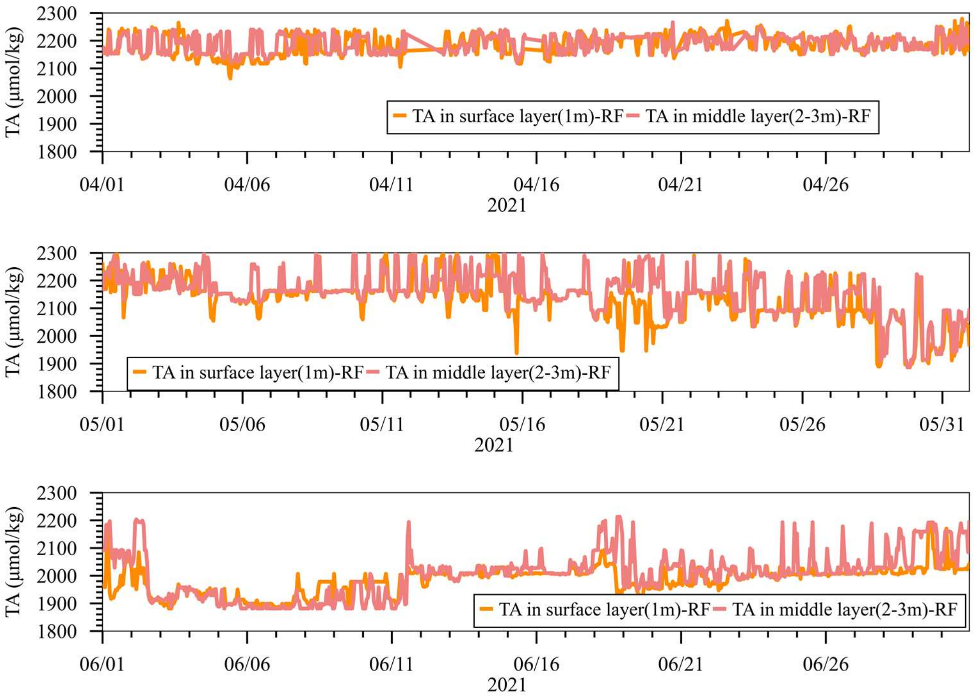

Figure 3.31 surface and middle layer Total alkalinity prediction result at Urayasu station using Random Forest model developed in this study

3.8.2 Time series $\mathbf{pCO_{2sw}}$

As shown in Figure 3.32, in most cases, the pCO_{2sw} is larger than the $pCO_{2\,air}$ that releasing of CO2 happens in most cases that this location is more likely to be regarded as a CO2 source, and the influence of Edo River water inflow as well as the upwelling at the head of the bay can be assumed as the reason. In January and February, $pCO_{2\,sw}$ is much larger than the $pCO_{2\,air}$ that the location was a strong source. Between Feb 5th and Feb 15th, also on around March 21st, low pCO_{2sw} in the seawater matched with phytoplankton bloom that it was the phytoplankton activity suppressed the pCO_{2sw} in seawater. From April to June, the fluctuation of pCO_{2sw} in seawater became much larger, which is thought to be caused by stronger biological activity, reflecting the day-night change. In June, from 25th to 29th, pCO_{2sw} in the seawater is suppressed by phytoplankton activity, but between June 11th to June 21st, even though bloom did not occur, the low pCO_{2sw} in seawater can still be observed, and this low pCO_{2sw} period matched with high pH condition in the seawater. It is assumed that south wind brought high pH ocean water into the bay. In addition, from May 7th to May 13th, phytoplankton bloom happened but the high pCO_{2sw} condition in seawater did not change, though river water inflow is considered as one reason, further study is needed to clarify the phenomenon.

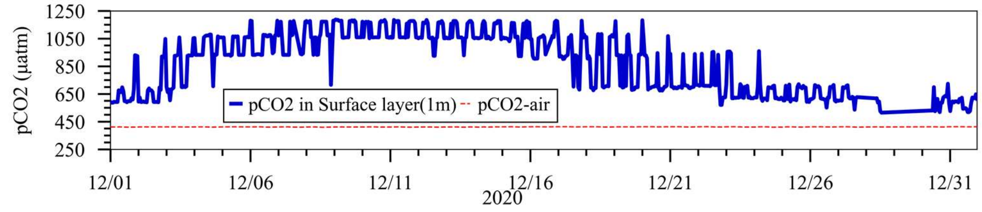
pCO2 (µatm)
1250
1050
850
650
450
250
pCO2 in Surface layer(1m)
pCO2-air
12/01
12/06
12/11
12/16
12/21
12/26
12/31
2020

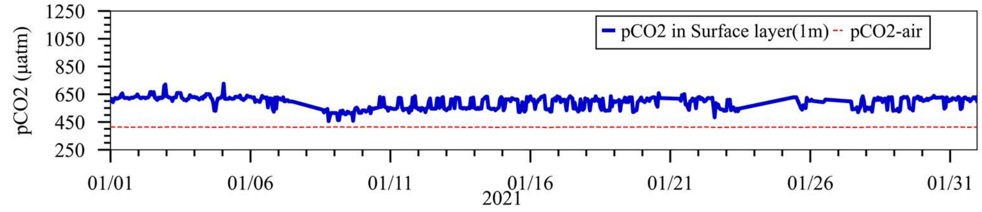
pCO2 (µatm)
1250
1050
850
650
450
250
pCO2 in Surface layer(1m)
pCO2-air
01/01
01/06
01/11
01/16
01/21
01/26
01/31
2021

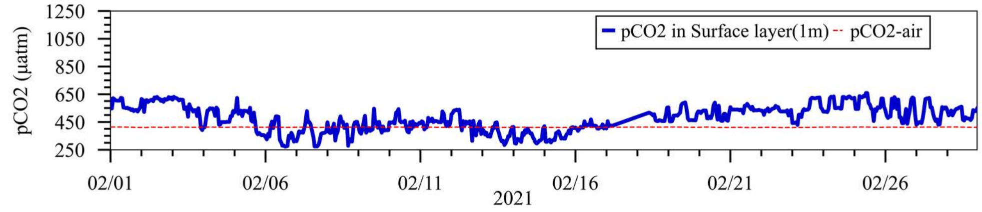
pCO2 (µatm)
1250
1050
850
650
450
250
pCO2 in Surface layer(1m)
pCO2-air
02/01
02/06
02/11
02/16
02/21
02/26
2021

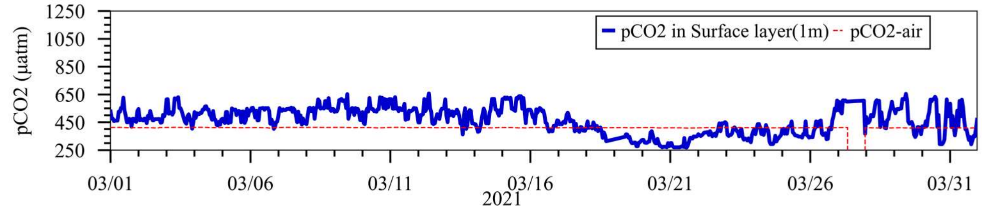
pCO2 (µatm)
1250
1050
850
650
450
250
pCO2 in Surface layer(1m)
pCO2-air
03/01
03/06
03/11
03/16
03/21
03/26
03/31
2021

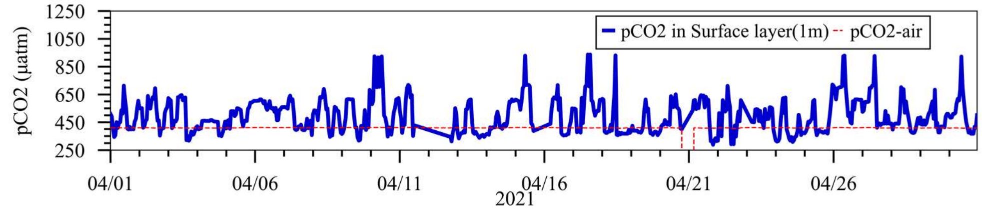
pCO2 (µatm)
1250
1050
850
650
450
250
pCO2 in Surface layer(1m)
pCO2-air
04/01
04/06
04/11
04/16
04/21
04/26
2021

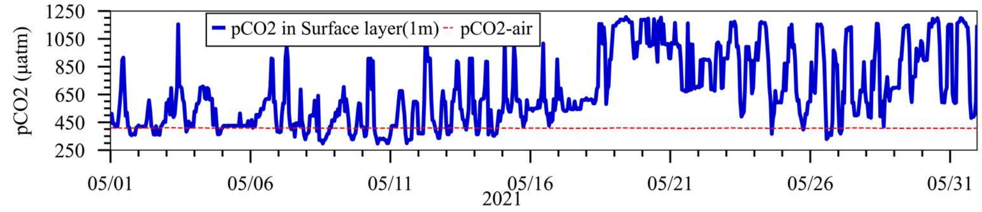
pCO2 (µatm)
1250
1050
850
650
450
250
pCO2 in Surface layer(1m)
pCO2-air
05/01
05/06
05/11
05/16
05/21
05/26
05/31
2021

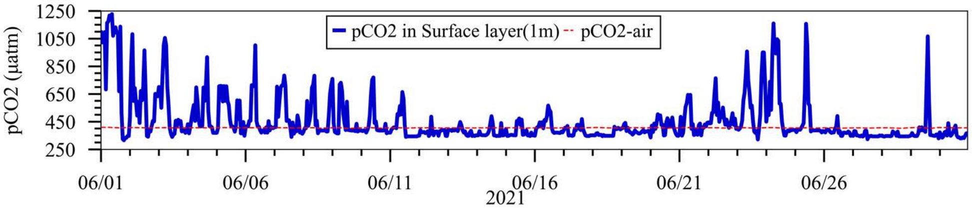

Figure 3.32 surface pCO_{2sw} prediction result at Urayasu station Using Gradient Boosting model developed in this study, and the calculation result of atmospheric pCO_{2sw}

pCO_{2sw} in the middle layer is also predicted as a comparison. Surveys conducted from bank reveals the pCO_{2sw} in the bottom layer will be higher than the surface layer under most cases [11], however, our prediction result shows that the pCO_{2sw} in the middle layer is very stable compared to the surface layer. It is the surface pCO_{2sw} fluctuating largely that falls below and rise above the pCO_{2sw} on the surface.

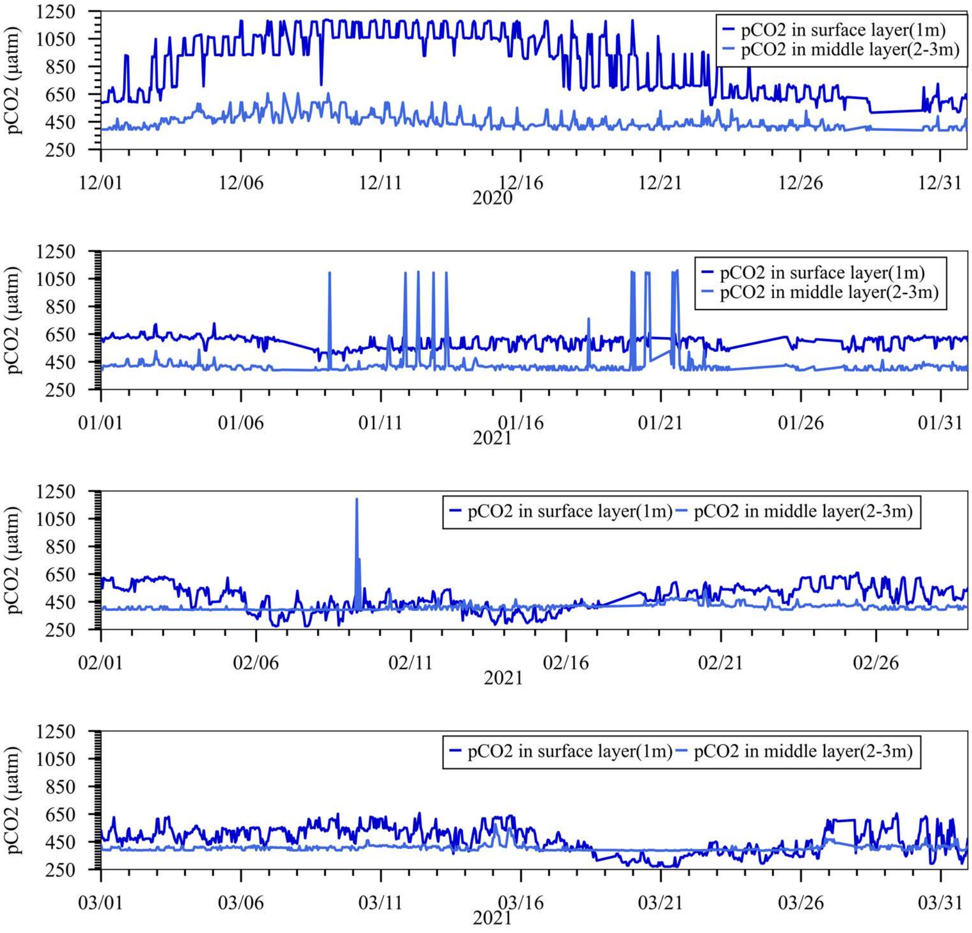

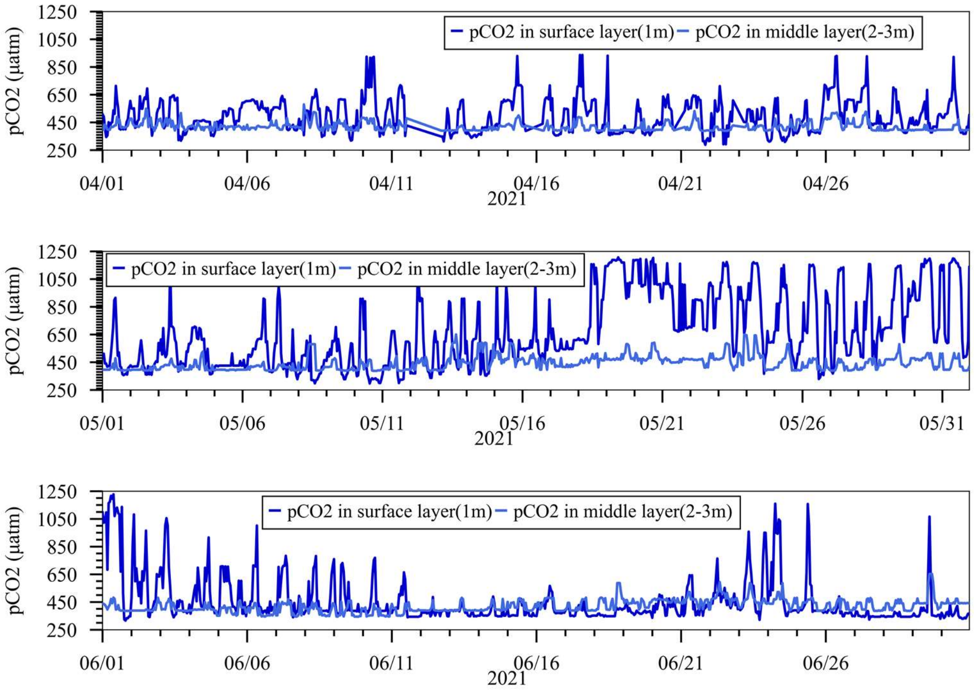

Figure 3.33 surface and middle layer $\mathrm{pCO}_{2\mathrm{sw}}$ prediction result at Urayasu station using Gradient Boosting model developed in this study

In addition, previous method for $\mathrm{pCO}_{2\mathrm{sw}}$ estimation by using the CO2SYS is also applied for comparison. $\mathrm{pCO}_{2\mathrm{sw}}$ in figure 3.32 and figure 3.34 has similar trend. In figure 3.32, under most case, $\mathrm{pCO}_{2\mathrm{sw}}$ is larger than $\mathrm{pCO}_{2\,\mathrm{air}}$. However, in figure 3.34, $\mathrm{pCO}_{2\mathrm{sw}}$ is lower than $\mathrm{pCO}_{2\,\mathrm{air}}$ in most instances, indicating an opposite conclusion that Urayasu is a sink for CO2.

Results from previous studies based on field survey [9] and numerical simulation [22] has the same conclusion with us that the Urayasu is a source for CO2 that the previous method using CO2SYS for $\mathrm{pCO}_{2\mathrm{sw}}$ estimation in the field may overstated bays' role as coastal blue carbon.

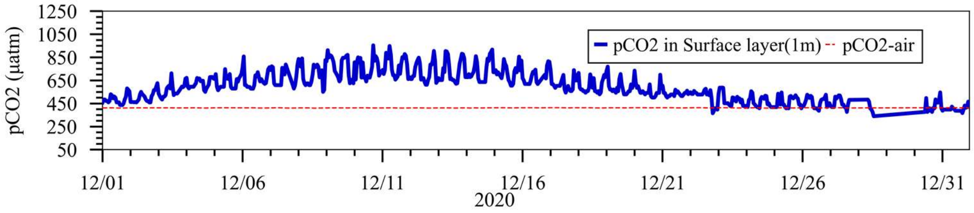

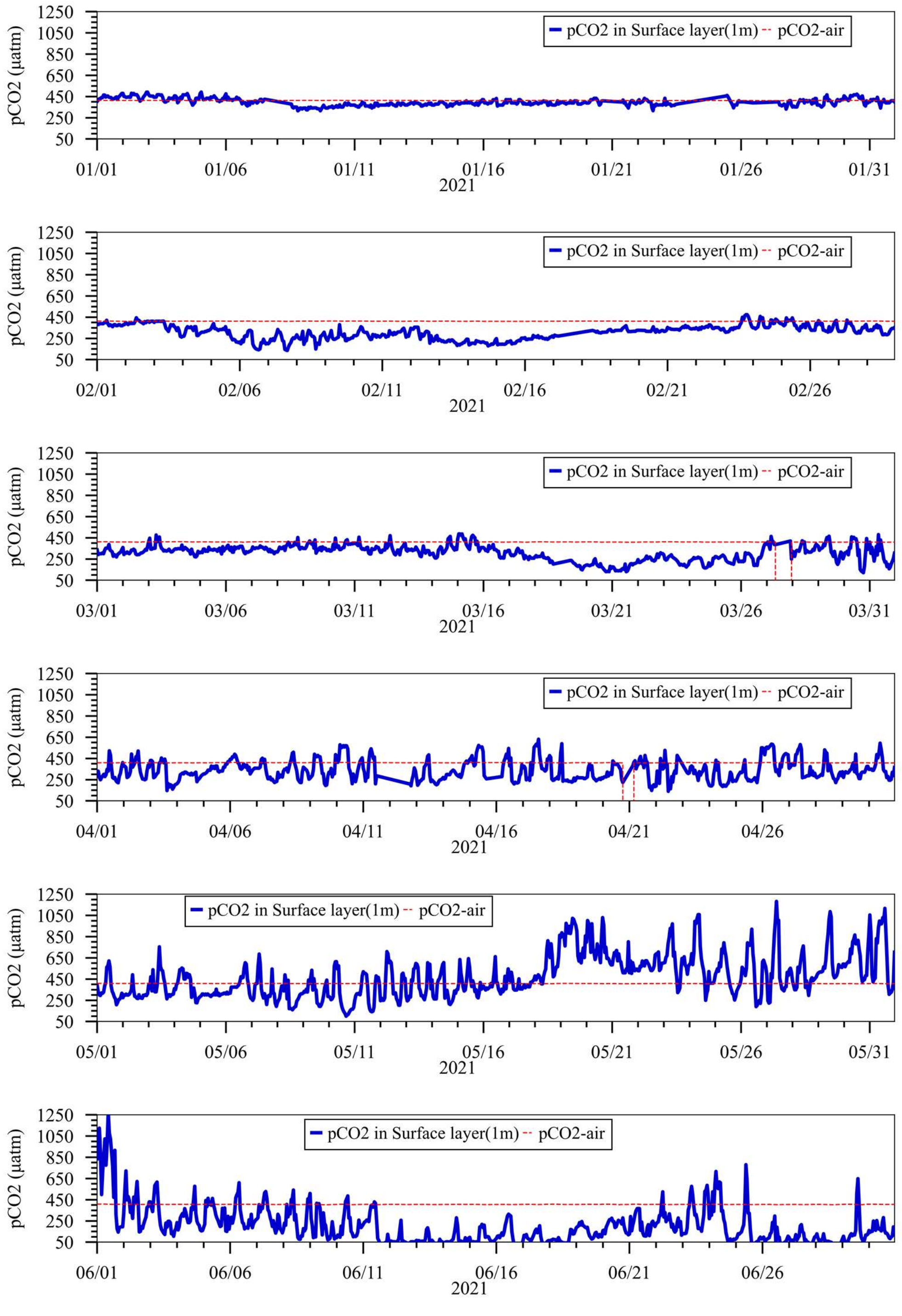

Figure 3.34 surface pCO_{2sw} prediction result at Urayasu station Using CO2SYS, and the calculation result of atmospheric pCO_{2sw}

3.9 Time series CO2 flux

3.9.1 Field survey results

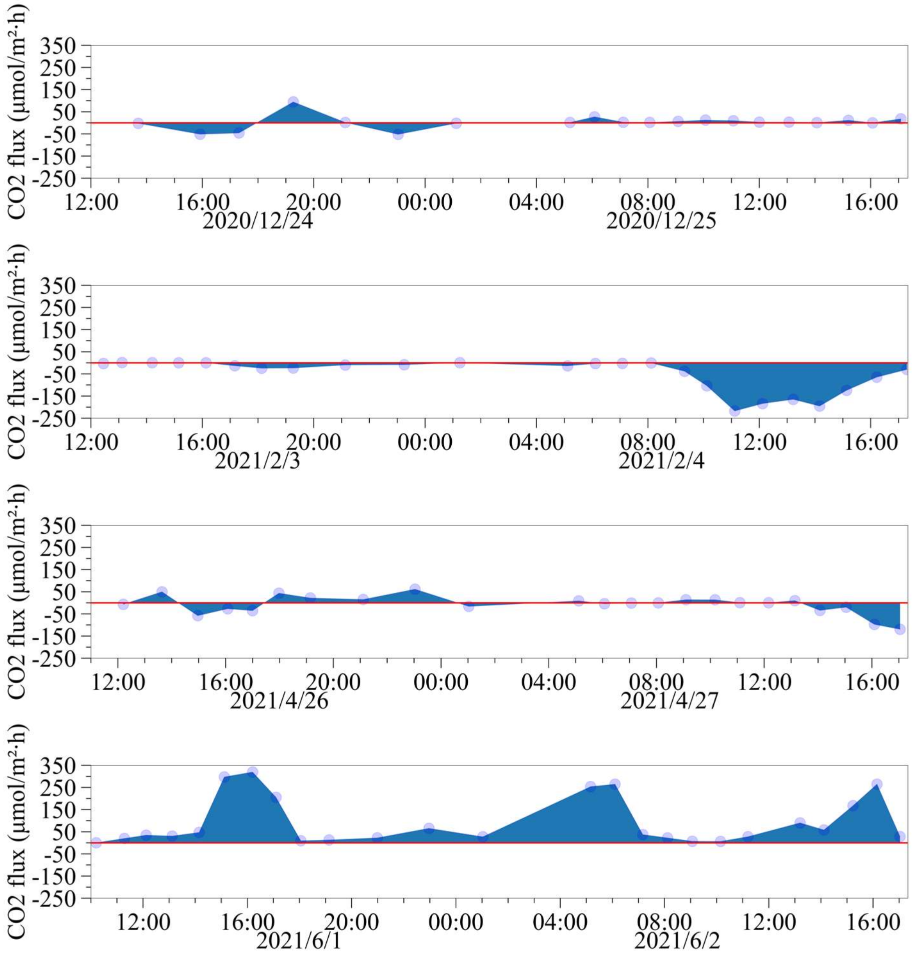

Figure 3.35 CO2 flux during field survey

Environment change influence on CO2 flux can be seen in figure 3.35. During the survey in December, it was low tide at around 19:00 on Dec 24th and 6:00 on Dec 25th, and the releasing of CO2 matched with the timing of river water inflow. On Feb.4th afternoon, strong south wind brought low CO2 concentration seawater to the field, resulting in absorption of CO2. Spring tide caused longer releasing period on April 26th during low tide, but photosynthesis caused absorption during high tide at around 16:00 on April 26th and 15:00 on April 27th. In the survey of June, because of rainfall, surface pH was smaller, leading to release of CO2, especially during low tide as river also collected rainwater. Respiration at night also lead to releasing of CO2. As a conclusion, seasonal change in CO2 flux cannot be seen from the field survey data. River water inflow, seawater movement, rainfall, photosynthesis, and respiration all have significant influence on CO2 flux trend, but this trend is strengthened or diminished by wind condition as explained in section 1.5. Therefore, compared to CO2 flux, $\mathrm{pCO_{2sw}}$ seems to be a better term to reflect the water environmental change influence.

3.9.2 Estimated results at Urayasu monitoring station

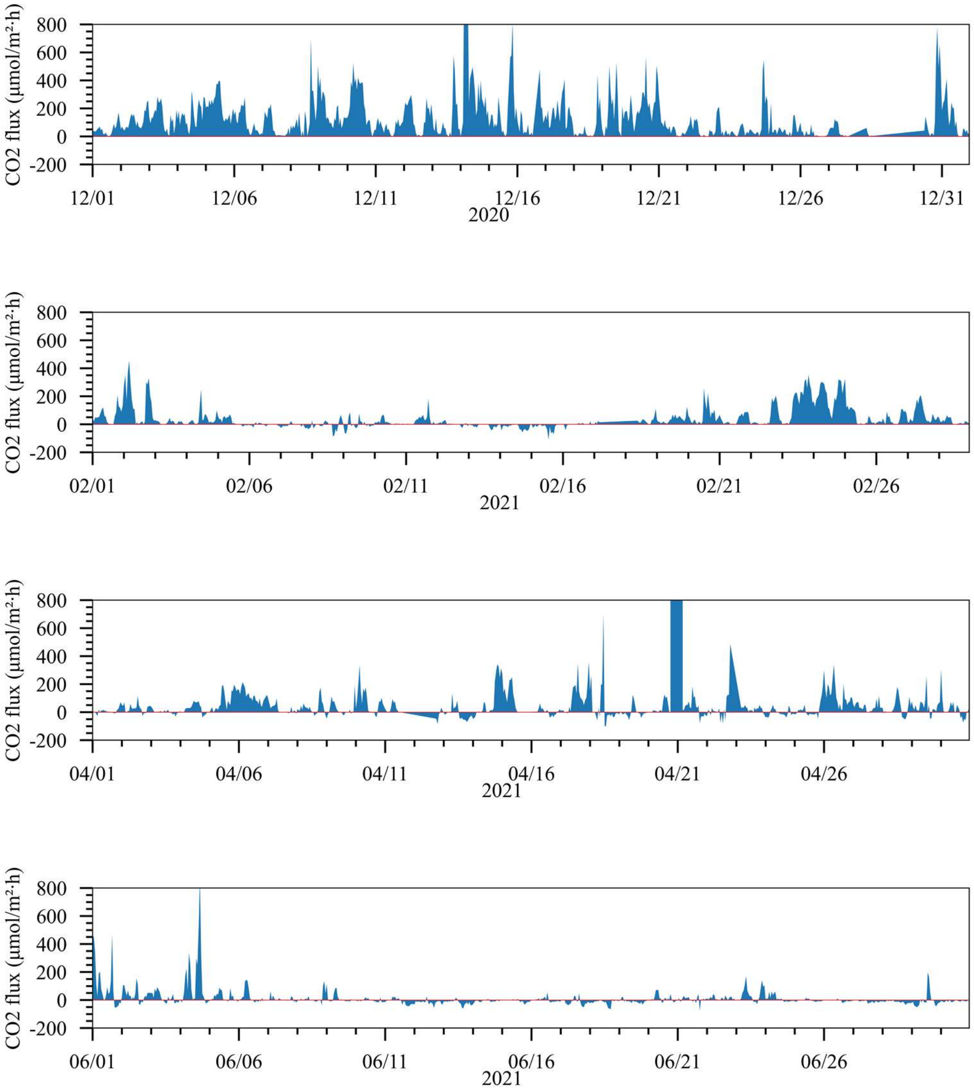

Figure 3.36 CO2 flux estimation result at Urayasu station

As a contract, long-term CO2 flux is estimated at Urayasu station to observe the seasonal change. No events happened in December and April, and the high spike on April 21st is due to missing data, as in figure 3.34. Urayasu acted as a source for CO2 continuously in December, but in April warmer water provided better condition for photosynthesis that CO2 releasing was weaker than in winter. Events happened in February and June. Bloom happened from Feb 5th to Feb 15th, and from June 25th to 29th, which caused absorption of CO2. Between June 11th to June 21st, south wind bringing lower CO2 concentration seawater into the bay is assumed to be another reason for absorption.

Chapter 4 Conclusion

In this research, the time-series sampling at the river mouth of Sakai River reveals that at sampling site, $\mathrm{pCO_{2sw}}$ is comparatively stable in winter, while largely fluctuates in spring due to active primary production. Environment change influence on seawater carbonate system including river water inflow, day-night change under different condition, biological process influence was observed. River water inflow caused $\mathrm{A_T}$, DIC and $\mathrm{pCO_{2sw}}$ all becoming larger in the coastal seawater, photosynthesis caused $\mathrm{pCO_{2sw}}$ in seawater to decrease suddenly, and the respiration caused significant $\mathrm{pCO_{2sw}}$ increase during nighttime. The location we chose for continuous sampling is enclosed by artificial structures, so the water at this location is more likely to be influenced by river water, and therefore a bit different from the seawater in the bay. The impacts of river water inflow are carefully studied.

A data driven approach is applied to utilize the biased field pH data to estimate field $\mathrm{pCO_{2sw}}$ accurately. With the data collected through experiment, the underestimation of $\mathrm{A_T}$ and $\mathrm{pCO_{2sw}}$ is noticed, and therefore new estimation method is proposed in this study. For $\mathrm{A_T}$ estimation, compared to the empirical equation that only uses salinity as an input, the temperature is added to reflect the seasonal change. The field measured pH inputted to CO2SYS[15] to calculate $\mathrm{pCO_{2sw}}$ in previous method is thought to be the cause of the underestimation of field $\mathrm{pCO_{2sw}}$, and to avoid this bias, a machine learning approach is applied to relate this measured pH to accurately calculated $\mathrm{pCO_{2sw}}$. With the data-driven approach, the bias between the predicted value and the true value became much smaller. In future work, $\mathrm{pCO_{2sw}}$ data covering the pivotal pH range will be collected to further improve the capability of this data-driven approach.

Location of Urayasu monitoring post is likely a source for CO2. The generalized $\mathrm{A_T}$ and $\mathrm{pCO_{2sw}}$ estimation method is furthermore applied using Urayasu monitoring data, which reflected seasonal change in seawater carbonate system fluctuation. This long-term estimation of CO2 exchange tend in Urayasu shows that this location is a source instead of a sink for atmospheric CO2. Though this conclusion matched with previous research, further study is needed to prove the reliability of predicted results, and the field $\mathrm{pCO_{2\,air}}$ needs to be measured to improve the accuracy of CO2 flux result.

Reference:

1. Core Writing, T., et al., *Climate change 2014 : synthesis report : A report of the Intergovernmental Panel on Climate Change*. 2014: IPCC. xvi, 151 p.
2. Nellemann, C., et al. *Blue Carbon : The Role of Healthy Oceans in Binding carbon. A Rapid Response Assessment*. 2008.
3. Mcleod, E., et al., *A blueprint for blue carbon: toward an improved understanding of the role of vegetated coastal habitats in sequestering CO2.* Frontiers in Ecology and the Environment, 2011. **9**: p. 552-560.
4. Duarte, C.M., et al., *The role of coastal plant communities for climate change mitigation and adaptation.* Nature Climate Change, 2013. **3**: p. 961-968.
5. Tang, J., et al., *Coastal blue carbon: Concept, study method, and the application to ecological restoration.* Science China Earth Sciences, 2018. **61**: p. 637-646.
6. Borges, A., B. Delille, and M. Frankignoulle, *Budgeting sinks and sources of CO2 in the coastal ocean: Diversity of ecosystems counts.* Geophysical Research Letters, 2005. **32**.
7. Chen, C., et al., *Ai' sea exchanges of CO 2 in the world's coastal seas.* Biogeosciences, 2013. **10**: p. 6509-6544.
8. 遠藤，徹., et al., *DIC の空間分布調査による大阪湾,播磨灘および英虞湾の* CO_2 *フラックスの評価.* 土木学会論文集. B2，海岸工学 Journal of Japan Society of Civil Engineers. 土木学会海岸工学委員会 編, 2018. **74**(2): p. I_1315-1320.
9. Kubo, A., Y. Maeda, and J. Kanda, *A significant net sink for CO2 in Tokyo Bay.* Scientific Reports, 2017. **7**.
10. 遠藤，徹., et al., *都市沿岸域の人工湿地における CO₂ フラックスの四季調査と CO₂吸収・放出量の推定.* 土木学会論文集 B2(海岸工学), 2015. **71**(2): p. I_1327-I_1332.
11. 遠藤，徹., et al., *大阪湾奥部における pCO₂の鉛直分布と大気海水間の CO₂ 交換の関係.* 土木学会論文集 B2(海岸工学), 2017. **73**(2): p. I_1231-I_1236.
12. 田口，二., et al., *沿岸海域のアルカリ度.* 沿岸海洋研究, 2009. **47**(1): p. 71-75.
13. Hassoun, A.E.R., et al. *Modeling of the Total Alkalinity and the Total Inorganic Carbon in the Mediterranean Sea*. 2015.
14. 遠藤，徹.，紘. 今吉, and 範. 原田, *水質連続モニタリングによる大和川河口域における* CO_2*交換特性の把握.* 土木学会論文集. B2，海岸工学 Journal of Japan Society of Civil Engineers. 土木学会海岸工学委員会 編, 2019. **75**(2): p. I_1165-1170.
15. Humphreys, M.P., et al., *PyCO2SYS v1.7: marine carbonate system calculations in Python.* Geosci. Model Dev. Discuss., 2021. **2021**: p. 1-45.
16. Dickson, A. *The carbon dioxide system in seawater : equilibrium chemistry and measurements*. 2011.
17. Dickson, A.G., C.L. Sabine, and J.R. Christian, *Guide to best practices for ocean CO[2] measurements*. PICES special publication. Vol. no. 3. 2007: North Pacific Marine Science Organization. 1 v. (various pagings).
18. Atkins, P.W., J. De Paula, and J. Keeler, *Atkins' physical chemistry*. 11th ed ed. 2018: Oxford University Press.

xxvii, 908 p.

19. Lewis, E., D. Wallace, and L.J. Allison, *Program developed for CO{sub 2} system calculations*. 1998, ; Brookhaven National Lab., Dept. of Applied Science, Upton, NY (United States); Oak Ridge National Lab., Carbon Dioxide Information Analysis Center, TN (United States). p. Medium: ED; Size: 40 p.
20. *国土交通省 関東地方整備局 東京湾環境情報センター 東京湾水質連続観測*. Available from: https://www.tbeic.go.jp/MonitoringPost/Top.
21. *ICSC 0979 - 塩化水銀(II) - ILO*.
22. 佐藤, 文., 淳. 佐々木, and A.A.W.R.R.M.K. Amunugama, *水底質統合モデルを用いた東京湾における炭素収支の推算と気候変動に伴う将来予測.* 土木学会論文集 B2(海岸工学), 2017. **73**(2): p. I_1441-I_1446.
23. アドバンテック株式会社, J., *直読式総合水質計 AAQ-RINKO 取扱説明書.*
24. *HOBO pH・温度データロガー(MX2501)取扱説明書.*
25. *U26-001 溶存酸素データロガー取扱説明書.*
26. 紀本電子工業株式会社, *全アルカリ度滴定装置 ATT-05 取扱説明書.*
27. Orr, J.C., J.M. Epitalon, and J.P. Gattuso, *Comparison of ten packages that compute ocean carbonate chemistry.* Biogeosciences, 2015. **12**(5): p. 1483-1510.
28. *PyCO2sys Validation*. External comparisons; Available from: https://pyco2sys.readthedocs.io/en/latest/validate/.
29. Lueker, T., A. Dickson, and C.D. Keeling, *Ocean pCO2 calculated from dissolved inorganic carbon, alkalinity, and equations for K1 and K2: validation based on laboratory measurements of CO2 in gas and seawater at equilibrium.* Marine Chemistry, 2000. **70**: p. 105-119.
30. Dickson, A., *Standard potential of the reaction: AgCl(s) + 1 2 H 2 (g) = Ag(s) + HCl(aq), and and the standard acidity constant of the ion HSO4− in synthetic sea water from 273.15 to 318.15 K.* The Journal of Chemical Thermodynamics, 1990. **22**: p. 113-127.
31. Uppström, L., *The boron/chlorinity ratio of deep-sea water from the Pacific Ocean.* Deep Sea Research and Oceanographic Abstracts, 1974. **21**: p. 161-162.
32. Perez, F.F. and F. Fraga, *Association constant of fluoride and hydrogen ions in seawater.* Marine Chemistry, 1987. **21**: p. 161-168.
33. *The NIST Reference on Constant, Units, and Uncertainty*. Fundamental Pysical Constants; Available from: https://physics.nist.gov/cgi-bin/cuu/Value?r.
34. Cai, W. and Y. Wang, *The chemistry, fluxes, and sources of carbon dioxide in the estuarine waters of the Satilla and Altamaha Rivers, Georgia.* Limnology and Oceanography, 1998. **43**: p. 657-668.
35. Brewer, P. and J.C. Goldman, *Alkalinity changes generated by phytoplankton growth1.* Limnology and Oceanography, 1976. **21**: p. 108-117.
36. Fraga, F. and X. Álvarez-Salgado, *On the variation of alkalinity during phytoplankton photosynthesis.* Ciencias Marinas, 2005. **31**: p. 627-639.

37. Ramosaj, B. and M. Pauly, *Asymptotic Unbiasedness of the Permutation Importance Measure in Random Forest Models.* ArXiv, 2019. **abs/1912.03306**.

38. Millero, F., K. Lee, and M.P. Roche, *Distribution of alkalinity in the surface waters of the major oceans.* Marine Chemistry, 1998. **60**: p. 111-130.

39. Noriega, C. and M. Araujo, *Carbon dioxide emissions from estuaries of northern and northeastern Brazil.* Scientific Reports, 2014. **4**.

40. 古屋 秀基，”東京湾湾奥部における二酸化炭素収支の変動特性に関する研究”，2014 年度東京大学大学院 新領域創成科学研究科 修士論文